Carbohydrate Polymers 315 (2023) 120963

Contents lists available at ScienceDirect

Carbohydrate Polymers

journal homepage: www.elsevier.com/locate/carbpol

Nanocellulose-assisted 3D-printable, transparent, bio-adhesive, conductive, and biocompatible hydrogels as sensors and moist electric generators

Dinesh K. Patel [a], Tejal V. Patil [b], Keya Ganguly [a], Sayan Deb Dutta [a], Ki-Taek Lim [a,b,*]

[a] Department of Biosystems Engineering, Institute of Forest Science, Kangwon National University, Chuncheon 24341, Republic of Korea
[b] Interdisciplinary Program in Smart Agriculture, Kangwon National University, Chuncheon 24341, Republic of Korea

ARTICLE INFO

Keywords:
3D printing
Bio-adhesive
Conductive
Motion sensor
Temperature responsiveness

ABSTRACT

Transparent hydrogels have found increasing applications in wearable electronics, printable devices, and tissue engineering. Integrating desired properties, such as conductivity, mechanical strength, biocompatibility, and sensitivity, in one hydrogel remains challenging. To address these challenges, multifunctional hydrogels of methacrylate chitosan, spherical nanocellulose, and β-glucan with distinct physicochemical characteristics were combined to develop multifunctional composite hydrogels. The nanocellulose facilitated the self-assembly of the hydrogel. The hydrogels exhibited good printability and adhesiveness. Compared with the pure methacrylated chitosan hydrogel, the composite hydrogels exhibited improved viscoelasticity, shape memory, and conductivity. The biocompatibility of the composite hydrogels was monitored using human bone marrow-derived stem cells. Their motion-sensing potential was analyzed on different parts of the human body. The composite hydrogels also possessed temperature-responsiveness and moisture-sensing abilities. These results suggest that the developed composite hydrogels demonstrate excellent potential to fabricate 3D-printable devices for sensing and moist electric generator applications.

1. Introduction

Hydrogel-based flexible sensors convert external stimuli, such as strain, temperature, pressure, and chemical changes, into detectable electronic signals (Amit et al., 2019; Li, Chen, et al., 2020; Liang et al., 2021; Liu, Niu, et al., 2022; Zhang, MohebbiPour, et al., 2021). These sensors have gained significant attention owing to their unique characteristics, including flexibility, confirmability, portability, and mechanical stability. However, most reported conductive hydrogel sensors are opaque because of non-transparent conducting fillers and carbonaceous resources (Jeong et al., 2020; Liu, Wang, et al., 2022). Transparent hydrogel sensors have been developed to enable direct visualization of the areas of interest and improve the aesthetics of devices. Conductive polymers are the commonly used transparent hydrogel sensors. However, their hydrophobicity hinders their miscibility during hydrogel synthesis (Chakraborty et al., 2018; Roy et al., 2022). Thus, the optimization of miscibility is challenging for developing a transparent conductive hydrogel for sensing applications. Ionic hydrogels provide an alternative option for stretchable, transparent, conductive, and biocompatible platforms for strain sensing applications. The abundant water moieties in ionic hydrogels provide a favorable environment for ionic conductance (Wang, Zhou, et al., 2018; Zhang et al., 2019). However, it was reported that the ion migration efficiency decreased during stretching, affecting the resistance of the ionic hydrogel (Dang et al., 2019). The weak mechanical strength and low strain sensitivity also restrict the applications of ionic hydrogels. Therefore, it is challenging to integrate all required characteristics into a single hydrogel. Different polymers, such as poly(vinyl alcohol), acrylate polymers, and poly(ethylene oxide), have been developed as transparent hydrogels for specific applications (He et al., 2022; Sun et al., 2022). Acrylate chitosan (CS) has appealing physicochemical properties, including adhesiveness and biocompatibility (Kolawole et al., 2018; Zanon et al., 2022). However, its weak mechanical strength must be improved. Incorporating different polymer materials or nanofillers to the acrylate CS matrix is one of the most effective ways to increase the mechanical properties. Zhu et al. developed a transparent and self-powered hydrogel for sensing applications using methacrylate CS modified by sodium alginate and polyacrylamide. The mechanical strength of the resulting hydrogels was enhanced owing to the formation of intensively cross-linked structures between acrylated CS and acrylamide (Zhu et al., 2022). Xu et al. improved the mechanical strength and conductivity of acrylate CS by grafting it with polypyrrole and mixing it with difunctional

* Corresponding author at: Department of Biosystems Engineering, Institute of Forest Science, Kangwon National University, Chuncheon 24341, Republic of Korea.
E-mail address: ktlim@kangwon.ac.kr (K.-T. Lim).

https://doi.org/10.1016/j.carbpol.2023.120963
Received 3 February 2023; Received in revised form 12 April 2023; Accepted 24 April 2023
Available online 27 April 2023
0144-8617/© 2023 Elsevier Ltd. All rights reserved.

polyurethane and carboxymethyl CS. However, polypyrrole grafting led to opaqueness (Xu et al., 2020).

Three-dimensional (3D) printing facilitates the fabrication of pre-designed and complex structures, whereas adhesiveness can secure the printed structures without additional tapes or glues (Heidarian et al., 2022). Because of external forces, soft electronic and wearable devices are highly susceptible to rapid and permanent damage. Many natural systems, including skin, tend to restore all functions after damage (Wang, Oh, et al., 2018). Inspired by this, self-healing hydrogel is advantageous for sensing applications. The self-healing and recovery features were achieved by reversibly cross-linked structures in the hydrogels (Li et al., 2015). Shape-memorable hydrogels are appealing materials for soft robotics, biomedicine, and microswimmer applications owing to their unique characteristics (Cong et al., 2020; Shang et al., 2019; Song et al., 2021). Temporary or weak interactions between hydrogel components are responsible for shape memory and shape-recovery functions. Nanomaterials, such as carbon, metal, oxide, and nanocellulose, have been extensively studied to develop stimuli-responsive shape-memory hydrogels (Li, Fu, et al., 2020). Among these nanomaterials, nanocellulose is considered a suitable filler to accelerate the shape memory and recovery of hydrogels and is often used to improve the mechanical strength (Patel et al., 2019; Zhou et al., 2022). The attractive physicochemical properties of nanocellulose include its light weight, low density, high mechanical strength, and biocompatibility. Nanocellulose has also been used to enhance the transparency of the developed materials (Gamage et al., 2020; Trache et al., 2020). Our group has demonstrated the biocompatibility of the spherical nanocellulose (s-NC)-based scaffolds. Improved wound healing and antibacterial potential have also been reported by our group using s-NC and carboxymethyl CS. However, the sensing potentials of these hydrogels have not been assessed (Patel, Ganguly, Hexiu, et al., 2022). Nanomaterials derived from bioresources, such as beta-glucan (BG), have been widely used in tissue engineering applications because of their bioactivity and biocompatibility (Bagal-Kestwal & Chiang, 2021; El Hosary et al., 2020). However, their potentials to sense motion, temperature, and humidity have yet to be comprehensively explored.

Considering the attractive characteristics of nanocellulose and BG, they were incorporated into methacrylate CS to develop transparent, 3D-printable, and bio-adhesive hydrogels. The synergistic effects of the two polysaccharides for sensing applications were examined. A lithium phenyl-2,4,6-trimethylbenzoylphosphinate (LAP) photo-initiator was used for ultra-violet (UV) light curing. The formation of self-assembled structures was monitored using small angle x-ray scattering (SAXS) analyses. The developed hydrogels exhibited improved viscoelasticity, recovery, adhesiveness, shape memory, and biocompatibility. The sensing ability of the developed hydrogels was evaluated on different human body parts. The temperature and moisture sensing potentials were also measured. Based on these results, the bioresource-derived hydrogels reported in this study have multiple functionalities and can be utilized to sense motion, temperature, and humidity in various environments.

2. Experimental section

2.1. Materials

CS (310–375 kDa, >75 % deacetylated), methacrylic anhydride, LAP, potassium hydroxide (Sigma Aldrich, USA), sodium chlorite, ammonium persulfate (APS) (Daejung Chemicals, Republic of Korea), acetic acid (99.7 %), hydrochloric acid (35 %), sulfuric acid (98.08 %) (mass/mass, Wako Chemicals, Republic of Korea), and sodium hydroxide (Junsei Chemicals, Japan) were used in this study. BG was extracted from *Grifola frondosa* powder (20–30 μm). Nanocellulose was extracted from pine wood powder (80 mesh, 177 μm). WST-8 dye was obtained from Cellrix® (MediFab Co., Ltd. Republic of Korea). All chemicals were used as purchased without further purification.

2.2. Functionalization of CS

Nanocellulose was isolated from pine wood powder as previously reported by our group. The detailed processes are provided in the Supplementary section. Water-soluble BG was extracted from *Grifola frondosa* powder as previously reported by our group. The detailed processes are described in the Supplementary section. CS methacrylamide (CSM) was synthesized as previously reported with some modifications (Alizadehgiashi et al., 2021). Briefly, CS was added to an acetic acid solution (1 %, v/v) under continuous mechanical stirring to obtain a homogenous CS solution (2 wt%). Subsequently, 0.8 mL of methacrylic anhydride was added dropwise. The mixture was then stirred for 7 h at room temperature and quenched by adding ice water. The solution was dialyzed against distilled water using a cellulose tube (MW: 12–14 kDa) for 5 d. The samples were dried in a freeze dryer (EYELA® Freeze Drying Unit 2200, Tokyo, Japan) for 72 h. The degree of methacrylation was calculated from its nuclear magnetic resonance (NMR) spectrum using the following equation:

$$Degree\ of\ methacrylation = \frac{A_{H(5.4\&5.8)}/2}{A_{H(2.7-4.0)}/5} \times Degree\ of\ chitosan\ deacetylation,$$

where $A_{H(5.4\&5.8)}$ is the peak area of methylene protons at 5.4 and 5.8 ppm, and $A_{H(2.7–4.0)}$ is the peak area of $_D$-glucose ring protons.

2.3. Synthesis of 3D-printable bio-adhesive hydrogels

A pure CSM hydrogel was prepared by adding CSM (5 wt%) in water. Similarly, the composite hydrogels of CSM/BG/nanocellulose were prepared. In brief, a suspension of s-NC (1, 2, and 4 wt%, w.r.t. to CSM) was mixed in a CSM matrix, followed by adding BG (1 wt%, w.r.t. to CSM). Subsequently, LAP (0.1 wt%) was added to the hydrogels and kept under dark conditions at 4 °C. The developed hydrogels were chemically cross-linked by a UV light (365 nm) for 5 min. The pure polymer- and BG/nanocellulose hydrogels are denoted as CSM and CSM/BG/s-NC-x, respectively, where x = 1, 2, and 4 is the amount of s-NC in the CSM polymer.

2.4. Characterizations

NMR spectroscopy (600 MHz, Bruker Avance Neo 600, Germany) was performed in deuterated water (D_2O) at room temperature to characterize the CSM. The Fourier transform infrared (FTIR), NMR (both proton and carbon), and mass characteristics of the extracted BG were reported in our previous study (Patel et al., 2020). The spectroscopic characterizations of the extracted nanocellulose were also presented in our previous work (Patel, Ganguly, Dutta, Patil, & Lim, 2023). The morphology of the isolated nanocellulose was examined using a field emission transmission electron microscope (FE-TEM) (JEM-2100F, Jeol, Japan). The surface charge of the isolated nanocellulose was assessed using a zeta potential particle size analyzer (Malvern, ZSP, UK). FTIR spectroscopy (Frontier, Perkin Elmer, UK) was used to assess the chemical interactions in the hydrogel in the wavelength range of 4000–500 with a resolution of 4 cm^{-1}. The total number of measurements was 32. The structural changes in the hydrogels were monitored *via* X-ray diffractometry (XRD; X'Pert PRO MPD, Philips, Eindhoven, Netherlands) with Cu Kα radiation (λ = 1.5414 Å) operated at a voltage of 40 kV and a current of 40 mA. The morphology of the printed constructs was examined using a scanning electron microscope (SEM) (Hitachi-S4800, Tokyo, Japan) with an acceleration voltage of 5.0 kV. Before the morphological examination, the printed constructs were freeze-dried using a freeze-dryer (EYELA® Freeze Drying Unit 2200, Tokyo, Japan) for 2 d and coated with platinum.

The self-assembly in the developed hydrogels was examined using

SAXS on a Xeuss 2.0 system with a sample-to-detector distance of 250 cm. The hydrogels were exposed for 600 s during the analyses. The viscoelasticity of the developed hydrogels was analyzed using an ARES-GE rheometer (TA Instruments, New Castle, Delaware, USA) on a 6 mm parallel plate at 25 °C. The mechanical strength of the prepared hydrogels was measured using a universal testing machine (UTM) (MCT-1150, A&D, Co. Japan) in compression mode with a compression speed of 10.0 mm/min.

2.5. 3D-printing

A CELLINK BIO-X printer was used to construct pre-designed 3D-structures on a sterile plate. The temperature of the printing bed was maintained at 25 °C. SolidWorks software (www.solidworks.com, Dassault Biosystems, France) was used to design the structures. Rectangular ($20 \times 20 \times 2\ mm^3$) structures were printed using a needle (22G) with a printing speed of 2 mm/s. The pressure was adjusted to 85–110 kPa. The uniformity factor (U) and expansion ratio (α) were calculated using the following equations.

$$\text{Uniformity factor (U)} = \frac{\text{Length of the printed strand}}{\text{Length of the theoretical design}}$$

$$\text{Expansion ratio } (\alpha) = \frac{\text{Filament diameter (d)}}{\text{Nozzle Diameter (D)}}$$

2.6. Self-healing and adhesive examinations

The self-healing potential of the hydrogel was examined by measuring the viscoelasticity of the healed hydrogel (10 min) using the rheometer at 25 °C (Guo et al., 2019). For this purpose, the hydrogel was cut into two pieces. Healing occurred when the two pieces were contacted without applying external stimuli. The viscoelasticity of the healed hydrogel was measured.

The lap-shear method was used to examine the adhesive strength of the hydrogel through the UTM measurements at room temperature (Patel, Ganguly, Dutta, Patil, Randhawa, & Lim, 2023). In brief, the hydrogel (70 mg) was sandwiched between two paper surfaces (15 mm × 15 mm) and left for 20 min. All experiments were performed in triplicate ($n = 3$), and an average was reported.

2.7. Shape-memory assessment

The hydration-assisted shape-memory behavior of the hydrogels was assessed using a cyclic bending method (Jing et al., 2019). A straight strip of the hydrogel was folded at a given angle (θ_i), and a pressure was applied to the folded structure for 30 s to achieve an appropriate deformation (θ_f). The shape-fixing ratio (R_f) was determined using the following equation.

$$Rf = \frac{\theta_f}{\theta_i} \times 100$$

The bent structures were placed in an aqueous medium for 30 s to regain the initial shape, and then, the residual angle (θ_p) was measured. The shape-recovery ratio (R_r) was calculated using the following equation.

$$Rr = \frac{\theta_f - \theta_p}{\theta_f} \times 100$$

2.8. Cytotoxicity assessment

The cytotoxicity of the hydrogel was assessed using human dermal fibroblast (HDF) cells following the method reported earlier (Dutta et al., 2021) with some modifications. Briefly, HDF cells (1.0×10^4) were treated with hydrogels and cultured in a 5 % CO_2 incubator at 37 °C for various durations. Groups without hydrogel treatment were used as controls. The old media was replaced with fresh media at 3 d intervals. After incubation, the cells were washed with PBS (two times), and WST-8 dye (10 μL) was added to the fresh culture media and further incubated for 2 h to form formazan. A spectrophotometer (Infinite® M Nano 200 Pro, TECAN, Switzerland) was used to measure the quantity of formazan at 450 nm. All experiments were performed in triplicate ($n = 3$) and the data were presented as the average optical density ± standard deviation. Statistical significance was set at $^*p < 0.05$.

Furthermore, the cell morphologies were visualized using an inverted fluorescence microscope (DMi8 Series, Leica Microsystems, Germany) after 24 h of incubation. HDF cells (4.0×10^4) were loaded into the hydrogels and incubated. Cells with a pure polymer (CSM) hydrogel were used as the control. After incubation, the cells were washed with PBS (two times) and fixed with a 4 % PFA solution. The fixed cells were rinsed with PBS and treated with 0.1 % Triton-X 100 for 10 min. The cells were then incubated with 1 % BSA solution for 1 h, followed by staining with 200 μL of F-actin for 20 min. The nuclei were stained by DAPI, and excess stain was removed by washing with PBS (three times). One drop of Prolong® Antifade mounting medium was added, and the images were captured under a microscope.

2.9. Antibacterial examination

A colony counting method was applied to examine the antibacterial property of the hydrogels against *Escherichia coli* (*E. coli*) (ATCC 10536) and *Staphylococcus epidermidis (S. epidermidis)* (ATCC 12228) (Patel, Ganguly, Dutta, Patil, Randhawa, & Lim, 2023). Briefly, bacteria colonies were suspended in nutrient broth under continuous stirring (150 rpm) and incubated at 37 °C overnight to obtain new bacterial colonies. A spectrophotometer was used to measure the optical density of the freshly cultured bacteria at 600 nm. The bacteria solution was then diluted 100 times, and 100 μL of the diluted bacteria was added to the nutrient broth containing 5 mL of the culture media with hydrogels (40 mg/mL). The groups without hydrogels were considered as control. After incubating at 37 °C for 24 h, 100 μL of the bacterial medium was taken and transferred onto agar plates and further cultured at 37 °C to form new colonies. Each experiment was performed in triplicate ($n = 3$).

2.10. Electrochemical and sensing analysis

The conductance potentials of the hydrogels were determined from the slope of the current-voltage (IV) curves using a Keithley 2460 source meter® at room temperature. The dimensions of the hydrogels are listed in Table S1. Conductance was calculated using the following equation.

$$\text{Conductance } \left(\frac{1}{R}\right) = \textit{Slope of } \frac{I}{V} \textit{ curve}$$

The strain-sensing ability of the hydrogels was monitored using a Keithley 2460 source meter® at 5 *V*. For human motion sensing applications, a hydrogel with a fixed dimension ($16.50 \times 4.30 \times 3.50\ mm^3$) was applied to different parts of the human body (finger, wrist, and knee) and connected with conducting wires. An individual (Age; 35, Sex; Male, and Ethnicity; Asian) was involved in human motion sensing experiments. The informed consent was taken from the human subject to use the photographs and conduct the experiments described in this study.

The wires were further connected to the Keithley 2460 source meter®. By moving the human body parts, the current change in the hydrogel was recorded by the source meter at different times. The relative change in resistance ($\Delta R/R_0$) of was calculated using the following equation:

$$\textit{Relative resistance change } \left(\frac{\Delta R}{R_0}\right) = \frac{(R_s - R_0)}{R_0} \times 100,$$

where R_0 and R_s are the hydrogel resistance before and after applying the strain, respectively.

The strain sensitivity of the hydrogels was determined based on the gauge factor (GF), which was calculated using the following equation.

$$Gauge\ factor\ (GF) = \frac{\left(\frac{\Delta R}{R_0}\right)}{\varepsilon},$$

where $\left(\frac{\Delta R}{R_0}\right)$ and ε are the changes in relative resistance and applied strain, respectively.

For letter recognition, the hydrogel was sandwiched between two polyethylene films and connected to a conducting wire. The wires were connected to a Keithley 2460 source meter® to record the current change during letter writing. For temperature sensing, the hydrogels were placed in a jacket and connected to conducting wires. The jacket was kept in a water bath, and the increase in temperature was monitored using a thermometer. The wires were connected to a source meter to record current changes during heating and cooling. The humidity-sensing ability was monitored by soaking the dried hydrogel in water for different periods, and the change in current was recorded. All experiments were conducted in triplicate ($n = 3$) and the average data were used to assess the sensing abilities of the hydrogel.

2.11. Statistical analysis

Statistical analyses were conducted with one-way ANOVA using Origin Pro9.0 software. The data are presented as average ± standard deviations (SD). Statistical significance was considered at $^{*}p < 0.05$, $^{**}p < 0.01$, and $^{***}p < 0.001$. A comparison was made between the control and experimental groups.

3. Results and discussion

3.1. Functionalization of CS and printability of the hydrogels

As shown in the TEM image in Fig. 1a, the isolated NC was spherical with an average diameter of 45.1 ± 1.2 nm, demonstrating the successful formation of s-NC *via* the APS hydrolysis. The zeta potential of the extracted s-NC was −35.1 mV, indicating the negatively charged functional groups in the backbone of the isolated material (Patel, Ganguly, Dutta, Patil, & Lim, 2023). FTIR spectroscopy was used to characterize the materials at different isolation steps, and the spectra are displayed in Fig. 1b. The extracted materials (hemicellulose, cellulose, and nanocellulose) had similar FTIR spectra owing to the structural resemblance. The absorption peaks at 3330, 2920–2850, and 1017 cm^{-1} were attributed to O—H, C—H stretching vibration, and C—O functional groups of the polysaccharides, respectively. However, the additional absorption peaks at 1707 and 1504 cm^{-1} in hemicellulose were associated with the carbonyl functional group (>C═O) of the xylan and other non-cellulosic components, respectively (Patel, Dutta, Ganguly, & Lim, 2021). By contrast, such absorption peaks were not observed in cellulose, indicating that the hemicellulose and non-cellulosic components were successfully removed through chemical treatment. The absorption peak at 1635 cm^{-1} in cellulose was ascribed to the adsorbed water (Aguayo et al., 2018). The characteristic peak at 1732 cm^{-1} in s-NC was related to >C═O functional groups generated by cellulose carboxylation during APS treatment. Fig. 1c shows the chemical reaction scheme for CS functionalization. CS contained many functional groups, including hydroxyl, amine, and acetyl, and methacrylic anhydride predominantly reacted with the amine groups of CS under acidic conditions to produce CSM. Fig. S1 illustrates the reaction mechanism. The NMR spectrum of CSM is shown in Fig. 1d, wherein the peaks at 5.4 and 5.8 ppm indicated the successful functionalization of CS with methacrylic anhydride, consistent with a previous study (Alizadehgiashi et al., 2021). The degree of substitution was approximately 10.5. Hydrogels were developed in an aqueous solution by adding different amounts of s-NC and 1 % of BG. The polymer chains were randomly oriented and interacted with the added nanomaterials presumably through hydrogen bonding and dipole–dipole interactions. After irradiation with UV light (365 nm) in the presence of LAP for 5 min, the randomly oriented polymer chains were self-assembled *via* chemical cross-linking of methylene moieties (Tan et al., 2016). Fig. 1e shows a schematic of the orientation of the hydrogel components before and after UV irradiation. The possible interactions between the hydrogel components are discussed later in the manuscript.

As shown in Fig. S2a, the developed hydrogels formed a thread-like structure during printing, which was favorable for printing applications. The hydrogel was easily extruded from the needle, exhibiting shear-thinning properties. Fig. S2b shows an image of the printed hydrogel. The printed structure maintained its morphology, suggesting that appropriate shear thickening had occurred after printing. Various parameters, such as hydrogel extrusion, shear thinning, and thickening, significantly affect printability. An appropriate shear thickening rate was required to maintain the adhesiveness between the printed layers. Otherwise, the printed morphology would be destroyed. Fig. 2a shows the 3D-printed structures of CSM, CSM/BG/s-NC 2, and CSM/BG/s-NC 4. All printed structures maintained their dimensional accuracy. The accuracy of the printed material was profoundly influenced by the printing parameters, structural design, and material properties (Patel, Dutta, Hexiu, et al., 2022). The uniformity factor (U) of the printed hydrogels was measured to examine their printability. As shown in Fig. 2b, the U values for CSM, CSM/BG/s-NC 1, CSM/BG/s-NC 2, and CSM/BG/s-NC 4 were 1.021, 1.019, 1.017, and 1.01, respectively. These values were close to 1, indicating the good printability of the hydrogels. The composite hydrogels exhibited a decreased U value (1.021 → 1.01) compared to that of the pure polymer (CSM) hydrogel, indicating that the printability was improved after introducing BG and s-NC. The strong interactions between the components in the composite hydrogel facilitated the re-solidification of the hydrogels at an appropriate rate after printing. In addition, adhesiveness, gravity, viscosity, and shear thinning and thickening properties also significantly influence the uniformity of printed hydrogels (Gao et al., 2018). It was reported that hydrogels with low viscosity and thixotropic potential exhibited poor U values.

The expansion ratio (α) was measured to validate the printability of the hydrogels, and the results are shown in Fig. 2c. The α values for CSM, CSM/BG/s-NC 1, CSM/BG/s-NC 2, and CSM/BG/s-NC 4 were 3.915, 3.91, 3.90, and 3.61, respectively. Compared to pure polymer (CSM) hydrogel, composite hydrogels had lower α values, demonstrating their improved printability. The stronger interactions between the hydrogel components enhanced viscosity and adhesiveness, which is discussed later in this manuscript. The improved viscosity and adhesiveness of composite hydrogels restricted the expansion of the printed filaments and facilitated printability (Dutta et al., 2021). It was reported that the printing pressure has more adverse effects on cellular activity than the other parameters such as nozzle diameter and chamber temperature (Malekpour & Chen, 2022). The highly viscous solution required high printing pressure, which negatively influenced cell survival rate as the high shear stress caused damage to cell membranes.

The surface morphologies of the 3D-printed hydrogels were examined using FE-SEM, and the corresponding images are shown in Fig. 2d. The intact bridges and junctions in the freeze-dried scaffolds indicated their structural stability. The pure polymer (CSM) exhibited nearly smooth surface morphologies, whereas the composite hydrogels had rough and porous surface. Fig. 2e shows the high-resolution morphologies of the printed scaffolds. The porous structure could facilitate ion transport, media exchange, and other processes, which were beneficial for different applications. Composite scaffolds with more pores in their structures were also ideal to fabricate moisture-assisted electric generators as these pores could rapidly transport ions (H^+/OH^-) and generate currents. The moisture-assisted electric generation potential of the

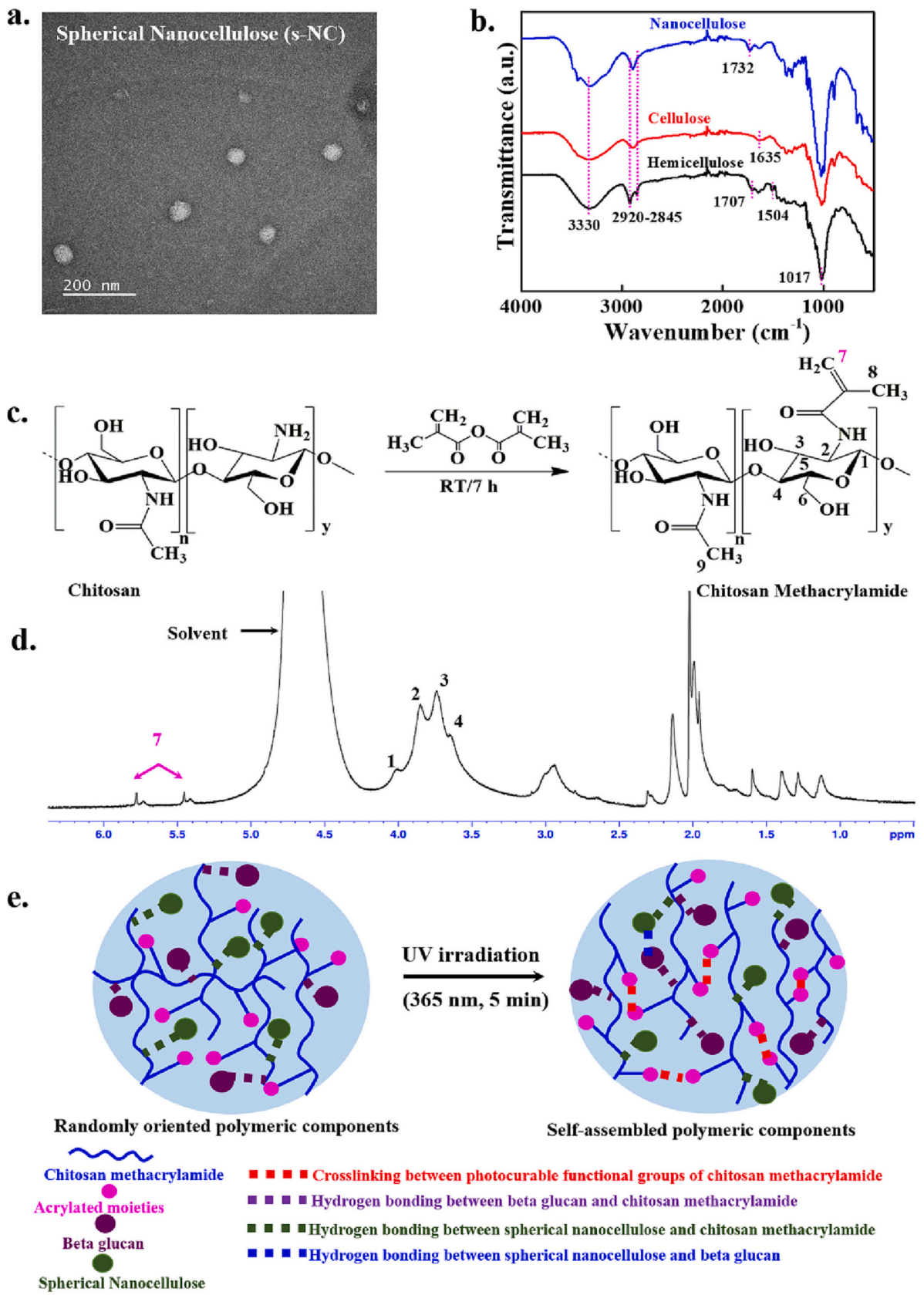

Fig. 1. **(a)** TEM image of isolated spherical nanocellulose (s-NC), **(b)** FTIR spectra of the indicated materials, **(c)** Surface functionalization of chitosan with methacrylic anhydride (n and y are respective repeating units), **(d)** NMR spectrum of functionalized chitosan, and **(e)** possible interactions between the hydrogel components.

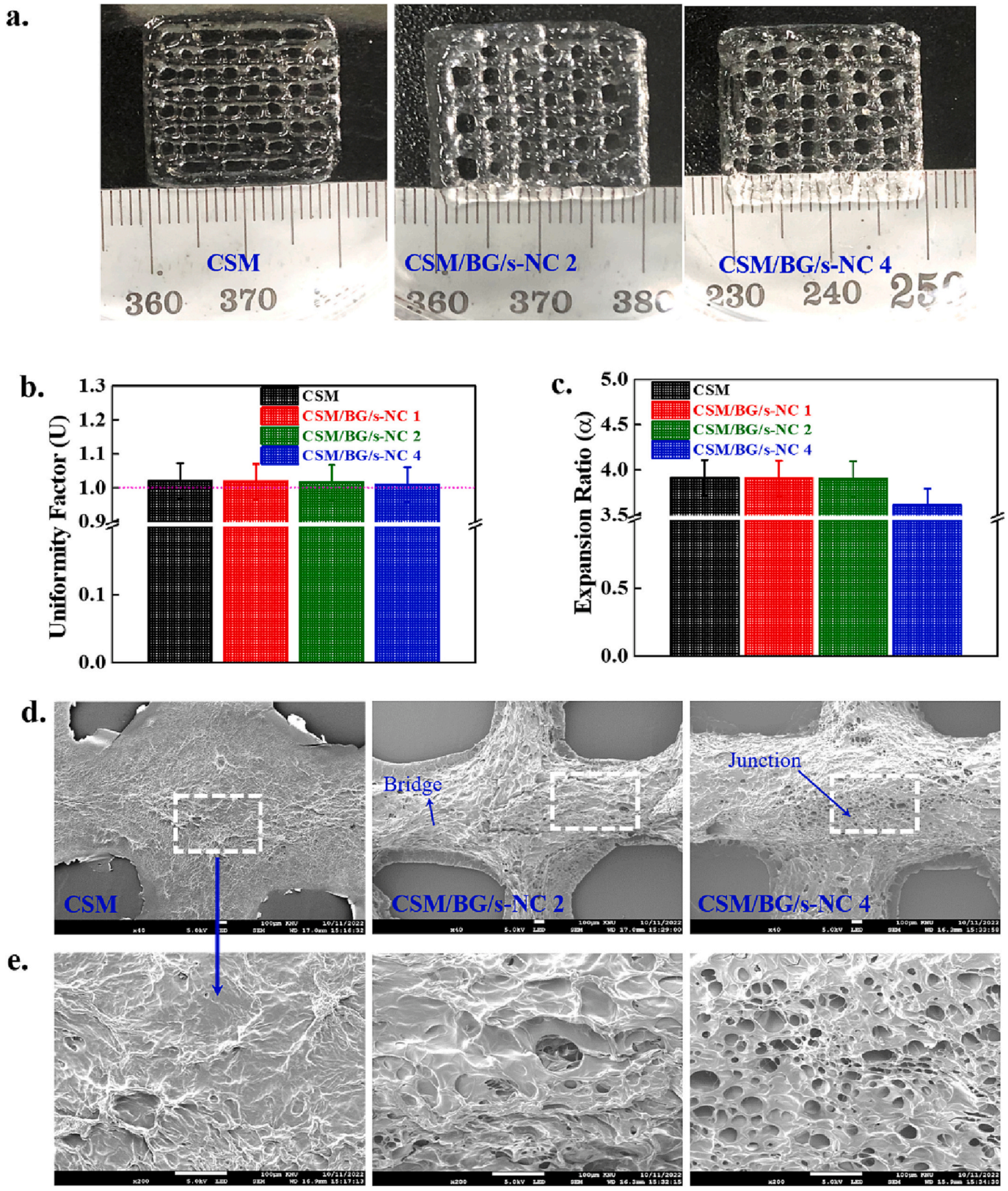

Fig. 2. Examination of the printability potential of the hydrogel. **(a)** 3D-printed hydrogels, **(b)** uniformity factor, **(c)** expansion ratio of the printed hydrogels, **(d)** SEM images of the printed scaffolds, and **(e)** high-resolution SEM images of the areas marked with a white-dotted square of the printed scaffolds.

scaffolds is discussed later in this manuscript. The swelling ability of the scaffolds was also examined, and the results are shown in Fig. S3. Compared to the swelling of pure polymer (CSM) scaffold (3270.0 %), the composite scaffolds showed enhanced swelling efficiency with a swelling of 6745.0 % after 2 h of incubation. The improved swelling ability was attributed to the presence of pores that facilitated water diffusion. However, the availability of functional groups and crystallinity also influenced the swelling properties (Patel, Ganguly, Hexiu, et al., 2022).

3.2. Structural elucidation and self-assembly phenomenon

As shown in Fig. 3a, the developed hydrogels were highly transparent. Fig. S4 presents the images of the letters KNU, wherein no significant difference was observed when the letters were covered or not covered with the hydrogel film. The quantitative transparency was determined using UV–vis spectroscopy, and the results are shown in Fig. 3b. The transparency of the pure polymer (CSM) film (0.14 mm) was >87 %, while the transparency of CSM/BG/s-NC 4 hydrogel was >85 % for both 0.14 and 0.18 mm thicknesses. A slight decrease in transmittance was observed in the 0.18 mm-thick film (85.51 %) compared to that in the 0.14 mm-thick film (85.8 %), suggesting that the transparency of the film could be increased by decreasing the film thickness. The electronic environment of the developed hydrogel was assessed using FTIR spectroscopy, and the spectra are shown in Fig. 3c. The broad absorption peak at 3315 cm^{-1} in pure CS was assigned to hydrogen-bonded amine/hydroxyl functional groups (Doshi et al., 2017). The absorption peaks at 1649 and 1559 cm^{-1} in CS were attributed to the stretching of carbonyl (>C═O) and the bending vibration of amide II (N—H) from the *N*-acetylated moieties, respectively. After functionalization, the intensity of the hydrogen-bonded amine/hydroxyl functional groups was significantly weakened and shifted towards higher wavenumbers (3315 → 3320 cm^{-1}), suggesting that some functional groups were consumed for functionalization. The weak absorption peak at 1421 cm^{-1} in pure CS was assigned to the symmetric vibration of carbonyl groups, which became prominent and shifted towards a lower

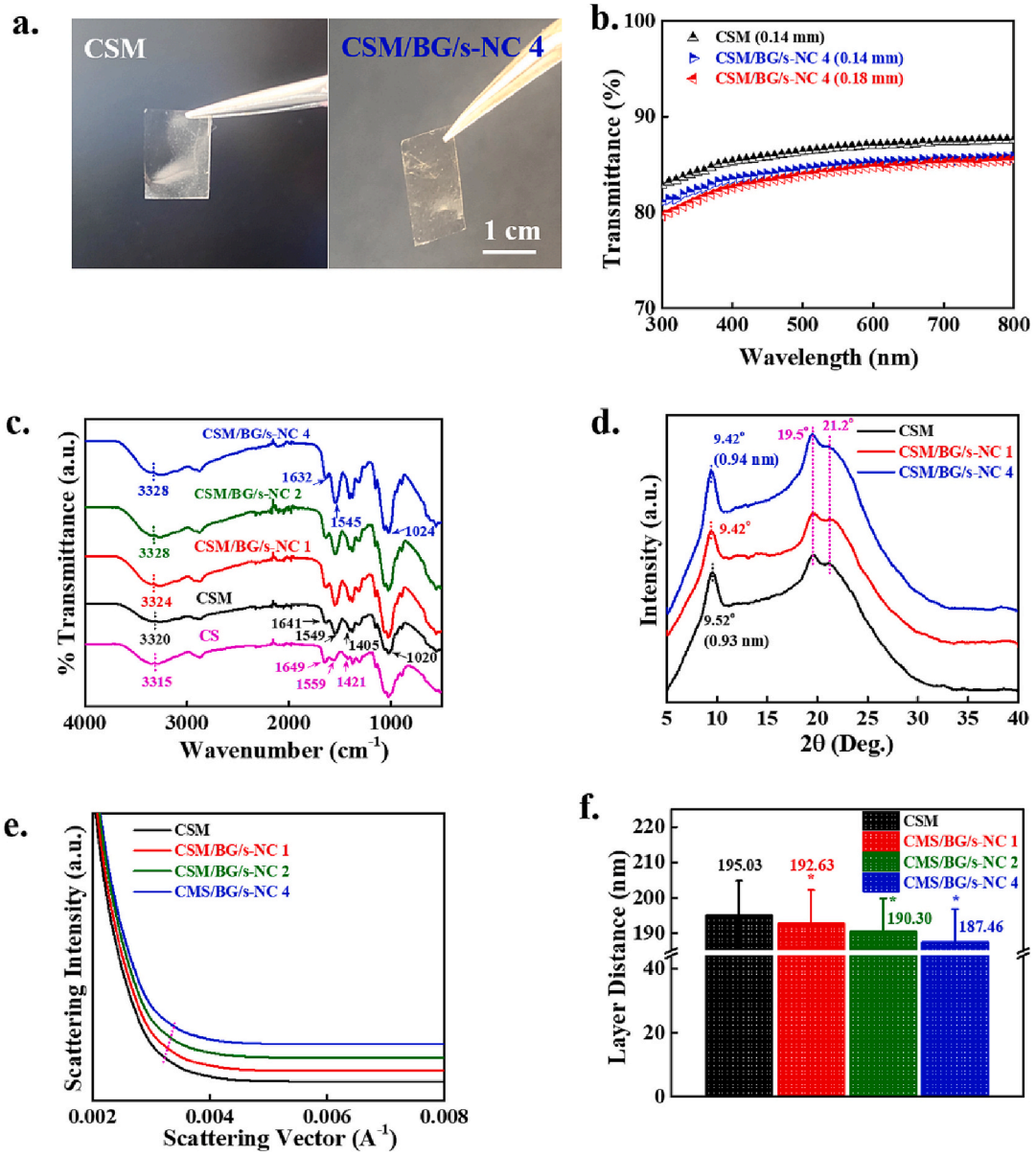

Fig. 3. Spectroscopic characterization and self-assembly behavior. **(a)** images of the indicated hydrogel film, **(b)** transmittance value of the indicated hydrogel films, **(c)** FTIR spectra of the hydrogel films, **(d)** XRD patterns of the indicated samples, **(e)** SAXS patterns of the indicated hydrogels, and **(f)** characteristic length of the indicated hydrogels.

wavenumber in CSM (1405 cm^{-1}) due to the grafting of methacrylic functional groups. These findings confirmed the successful functionalization of CS in CSM. A significant shift in the hydrogen-bonded amine/hydroxyl functional groups was observed in the composite hydrogels (3320 → 3328 cm^{-1}) because of the interactions between polymer chains and the added nanomaterials (BG and s-NC). Such interactions also caused a shift in amide I (1641 → 1632 cm^{-1}) and amide II (1549 → 1545 cm^{-1}). The developed hydrogels contained abundant polar hydroxyl and carbonyl groups. Therefore, dipole–dipole interaction and hydrogen-bonding are expected to play significant roles in these shifts (Lungu et al., 2021). Additionally, the composite hydrogels exhibited remarkably higher absorption intensity at 1024 cm^{-1}(C—O—C stretching) compared to the pure CSM polymer, due to the abundant C—O—C moieties in the added nanomaterials.

XRD was used to explore the effects of the added nanomaterials on the crystallinity of the CSM hydrogel. As shown in Fig. 3d, the pure CSM polymer exhibited diffraction patterns at 9.52, 19.5, and 21.2°, which were assigned to the (020), (220), and (200) reflection planes, respectively (Aziz et al., 2015). The sharp diffraction peak at 9.52° in CSM with an interplanar distance of 0.93 nm suggested the existence of crystalline patterns. The broad diffraction peaks at 19.5 and 21.2° in the CSM indicated amorphous zones. No significant changes in the diffraction peaks were observed in the composite hydrogels, demonstrating that the nanomaterials did not alter the structure of the pure polymer (CSM). However, a slight enhancement in the intensity of the diffraction peaks at 9.42 and 19.5° was observed at a higher nanomaterial content (4 wt %). This enhancement was due to the presence of crystalline nanomaterials in the hydrogels (Patel, Ganguly, Dutta, Patil, & Lim, 2023).

The formation of nanocrystalline structures *via* self-assembly in the developed hydrogels was further investigated using SAXS, which could provide significant information in the nanometer range (Ahn et al., 2019). As shown in Fig. 3e, a weak hump was observed in the developed hydrogels, demonstrating the presence of nanocrystalline structures. The interaction between different functional groups (—OH and >C═O) of the hydrogel components led to the formation of a self-assembled structure (Heiner et al., 2023). It was anticipated that the randomly oriented polymer chains would exhibit an ordered structure after UV irradiation as the photocurable functional groups of CSM could facilitate the self-assembly. The characteristic length ($\Lambda_c = 2\pi/q$) of the formed nanostructure was also determined to assess the molecular sheet required for self-assembly in the developed hydrogels. As shown in Fig. 3f, compared to the characteristic length of pure polymer (CSM)

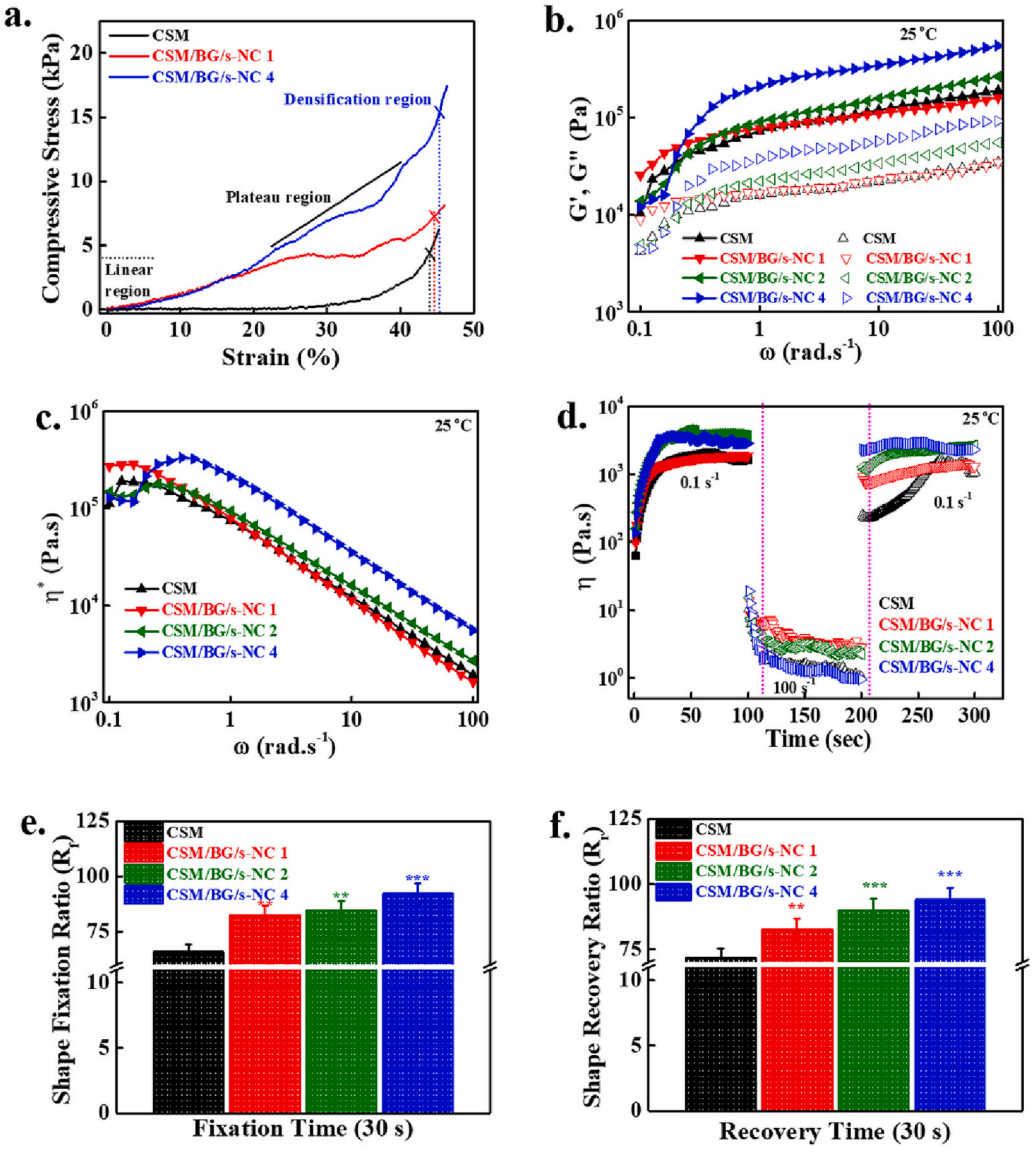

Fig. 4. **(a)** Stress-strain curves of the indicated hydrogels, **(b)** Storage and loss modulus of the hydrogels, **(c)** complex viscosity of the indicated hydrogels, **(d)** thixotropic behavior of the hydrogels, **(e)** shape fixation ability, and **(f)** shape recovery potential of the hydrogels.

hydrogel (195.03 nm), the composite hydrogels had a decreased characteristic length (187.46 nm), indicating the formation of more ordered structures. The characteristic length was further decreased by increasing the nanomaterial content owing to the strengthened interactions between the polymer chains and nanomaterials. Therefore, the abundant functional groups in s-NC and BG prompted the formation of self-assembled structures.

3.3. Mechanical strength and shape memory behavior

The mechanical strength of the developed hydrogels was assessed by UTM under compression mode, and the obtained stress–strain curves are presented in Fig. 4a. The hydrogels demonstrated a linear elastic region at low stress, followed by a plateau and a densification region similar to the porous materials. By measuring the slope of the stress–strain curves at the linear elastic region, the compressive moduli for CSM, CSM/BG/s-NC 1, and CSM/BG/s-NC 4 hydrogels were determined as 0.003 ± 0.0003, 0.123 ± 0.001, and 0.15 ± 0.001 kPa, respectively. The composite hydrogels showed improved mechanical strength compared to that of the pure polymer (CSM). The enhancement in the mechanical strength was attributed to the strong interactions between the added nanomaterials and polymer matrix, which facilitated the load transfer during the compression (Patel, Ganguly, Dutta, et al., 2022). Dipole–dipole interactions and hydrogen-bonding between the added nanomaterials (BG and s-NC) and polymer chains (CSM) were presumably major interactions responsible for the enhanced mechanical strength. The compressive strengths were 6.21 ± 0.3, 8.14 ± 0.4, and 17.48 ± 0.25 kPa for CSM, CSM/BG/s-NC 1, and CSM/BG/s-NC 4 hydrogels, respectively. The crack propagation process was suppressed by the added nanomaterials during the measurement, which enhanced mechanical strength (Liu et al., 2018). The composite hydrogels also showed lower densification strains (44.6 ± 0.8 and 45.3 ± 0.5 % for CSM/BG/s-NC 1 and CSM/BG/s-NC 4 hydrogels, respectively) than that of the pure CSM polymer (43.8 ± 0.16).

A rheometer was used to examine the viscoelasticity of the hydrogels at 0.1–100 rad/s and 25 °C and the results are presented in Fig. 4b. The hydrogels demonstrated solid-like characteristics, as no crossover point was observed in the measured range. The composite hydrogels, compared to the pure polymer (CSM) hydrogels, had an improved storage modulus (G′, solid lines) in the measured regions. This elastic property was further enhanced by increasing the nanomaterial content because sufficient interactions were involved between the hydroxyl-rich nanomaterials and polymer chains. Hydrogen bonding and dipole-dipole interactions were reported as reasons for the enhancement of the storage modulus of hydrogels (Xu et al., 2019). The nanocellulose-assisted enhancement of hydrogel viscoelasticity through hydrogen bonding was also reported (Liu et al., 2020). In the higher frequency region in Fig. 4b, an approximately 2.9-fold enhancement (188.2 → 546.7 kPa) in the storage modulus was observed in the composite hydrogels, compared to the pure polymer (CSM) hydrogel. This enhancement in the storage modulus at a high angular frequency could be explained by the relaxation and simultaneous reformation of the highly interconnected networks, which hindered the movement of the polymer chains, led to a solid-like property and improved storage modulus (Patel, Dutta, Shin, et al., 2021; Pati et al., 2014). The composite hydrogels had a higher loss modulus (G″, unshaded symbols without lines) than the pure polymer (CSM) hydrogel. However, their values were lower than the storage modulus in the measured regions, suggesting crosslinked network structures within the hydrogels.

Fig. 4c shows the changes in the complex viscosity (η*) values of the hydrogels in the measured regions. The composite hydrogels had a higher η* compared to the pure polymer (CSM) hydrogel, indicating their solid-like characteristics. The η* value was further enhanced by increasing the nanomaterial content in the polymer matrix as the stronger interaction within the hydrogel components generated a more compact structure. An increased η* value was observed in the hydrogels in the lower angular frequency regions, whereas a systematic decrease in η* occurred in the higher angular frequency regions, indicating shear thickening and thinning characteristics. These properties were essential for 3D printing applications (Schwab et al., 2020). The interaction between the hydrogel components facilitated the proper entanglement of randomly oriented polymer chains, forming a solid-like structure, and generating shear-thickening properties in the lower angular frequency region. The disentanglement of the polymer chains at a higher angular frequency minimized the interactions between the hydrogel components and decreased the viscosity, which was responsible for the shear thinning characteristic (Shan et al., 2015). The changes in the damping factor (tan δ) of the hydrogels at 0.1–100 rad/s and 25 °C were further analyzed, and the results are presented in Fig. S5. The damping factor provides significant information regarding the internal structure of the materials. A high tan δ value indicates a viscous characteristic, whereas a lower value indicates elastic properties (Liang et al., 2019). Compared to CSM, CSM/BG/s-NC 4 exhibited a decreased damping factor throughout the measured regions, demonstrating its enhanced elasticity owing to the stronger interactions between the hydrogel components. Thixotropic measurements were also performed to assess the recovery ability of the hydrogels after deformation, and the results are presented in Fig. 4d. The viscosity (η) of the hydrogels was measured at different shear rates of 0.1, 100, and 0.1 s^{-1} at 25 °C. At a low shear rate (0.1 s^{-1}), the η values for CSM, CSM/BG/s-NC1, and CSM/BG/s-NC 4 were 1628.8, 1861.04, and 2841.17 Pa·s, respectively. A high shear rate was applied to deform the crosslinked structures, which decreased its viscosity. After removing the high shear rate, the hydrogels recovered their initial viscosity. The recovered η values for CSM, CSM/BG/s-NC 1, and CSM/BG/s-NC 4 were 1064.7, 1291.21, and 2313 Pa. s, respectively. The recovery rates for CSM, CSM/BG/s-NC 1, and CSM/BG/s-NC 4 were 65.3, 69.2, and 81.4 %, respectively. The higher recovery rates in the composite hydrogels were attributed to the formation of more crosslinked structures through stronger interactions within the hydrogel after the removal of the shear rate. Recoverable hydrogels have received significant attention for the development of sensing devices; therefore, the excellent recovery characteristics of the composite hydrogels developed in this study demonstrated their great potential as novel sensing materials.

Furthermore, the hydration-assisted shape-memory behavior of the hydrogels at room temperature was examined. Fig. S6 presents the images of the hydrogel strip under different conditions (initial, temporary, and recovered). After immersion in water for 30 s, the hydrogel strips returned to their initial shapes. The composite hydrogels showed better recovery ability than the pure polymer (CSM), demonstrating their improved shape memory ability. Applying a certain pressure on the polymer strip resulted in a disordered structure because the asymmetric distributions of the functional groups generated a temporary structure. After hydration, the polymer strips behaved like hydrogel platforms, and their viscoelasticity characteristics governed their shape-recovery ability (Nissenbaum et al., 2020; Shang et al., 2019). Fig. 4e shows the quantitative shape-fixing (R_f) ability of the hydrogels. The R_f values for CSM, CSM/BG/s-NC 1, CSM/BG/s-NC 2, and CSM/BG/s-NC 4 were 65.8, 82.5, 84.5, and 92.2, respectively. The improved R_f values of the composite hydrogels were attributed to the formation of more disordered structures (amorphous zones). The higher asymmetric orientations of the active functional groups resulted in a more stable temporary structure. Fig. 4f shows the quantitative shape recovery (R_r) potentials of the hydrogels, which were 71.7, 82.6, 89.8, and 93.9 for CSM, CSM/BG/s-NC 1, CSM/BG/s-NC 2, and CSM/BG/s-NC 4, respectively. The increased R_r of the composite hydrogels were attributed to their superior viscoelastic properties, as discussed earlier. The enhanced viscoelasticity of the composite hydrogels accelerated shape recovery, consistent with the previous report (Wang et al., 2019).

3.4. Self-healing and adhesiveness of the hydrogels

The self-healing ability of the hydrogels was assessed using a rheometer, and the change in the storage modulus of the hydrogel after 10 min of the healing process is shown in Fig. 5a. The healed hydrogel possessed similar viscoelastic characteristics to the original hydrogel, indicating an effective healing process. The hydrogel recovered approximately 80.0 % of its initial storage modulus after 10 min of healing. This value might be further increased by increasing the healing time. Adhesive hydrogels have received significant interest for the development of wearable electronic devices because additional adhesive materials, such as bandages or tapes, may create allergic reactions. The adhesive ability of the hydrogels on different surfaces, including human skin, Eppendorf tubes, glass, and plastic surfaces, was assessed. As shown in Fig. 5b (i–iv), the developed hydrogels adhered adequately to various surfaces. The quantitative adhesiveness of the hydrogels was evaluated using the lap shear method, and a schematic of the measurement is shown in Fig. 5c. The adhesiveness of the hydrogels was measured using UTM, and the load *vs.* displacement curves are presented in Fig. S7. The composite hydrogels showed enhanced load-bearing potential compared to pure polymer (CSM) hydrogel because the stronger interactions between the applied surface and the active functional groups of the hydrogels increased the adhesiveness. The load-bearing efficiency of the hydrogels increased with an increasing nanomaterial content in the polymer matrix. Fig. 5d shows the adhesive strength *vs.* displacement curves of the hydrogels. The composite hydrogels demonstrated better adhesiveness as their adhesiveness was enhanced compared to that of the pure polymer (CSM) hydrogel. The adhesiveness further increased with an increasing nanomaterial content. The adhesiveness of the materials was affected by different factors, such as adhesion time, surface characteristics of the materials, physico-chemical properties of the hydrogels, and temperature (Dong et al., 2021).

Fig. 5e presents that the adhesive strengths were 64.6, 131.0, 148.8, and 157.5 kPa for CSM, CSM/BG/s-NC 1, CSM/BG/s-NC 2, and CSM/BG/s-NC 4, respectively. These values were significantly higher than those reported for nanocellulose-based hydrogels, indicating that the CSM/BG/s-NC composite had excellent adhesiveness for strain-sensing applications (Patel, Ganguly, Hexiu, et al., 2022; Qu et al., 2021; Wang, Dai, et al., 2021). The adhesiveness of the hydrogels might be further improved by applying polar surfaces with charged functional groups (COO^- and NH_3^+) in their structure, such as human skin, to facilitate interfacial interactions. Fig. 5f presents a possible mechanism for the interaction between the human skin and the hydrogel. Hydrogels with abundant hydroxyl moieties could strongly interact with the charged functional groups (COO^- and NH_3^+) of the peptide chains of human skin through hydrogen bonding, dipole-dipole, ion-dipole, and electrostatic interactions, improving adhesiveness. Lu et al. fabricated nanocellulose-assisted adhesive hydrogels for skin sensor applications using a radical-induced method (Lu et al., 2020).

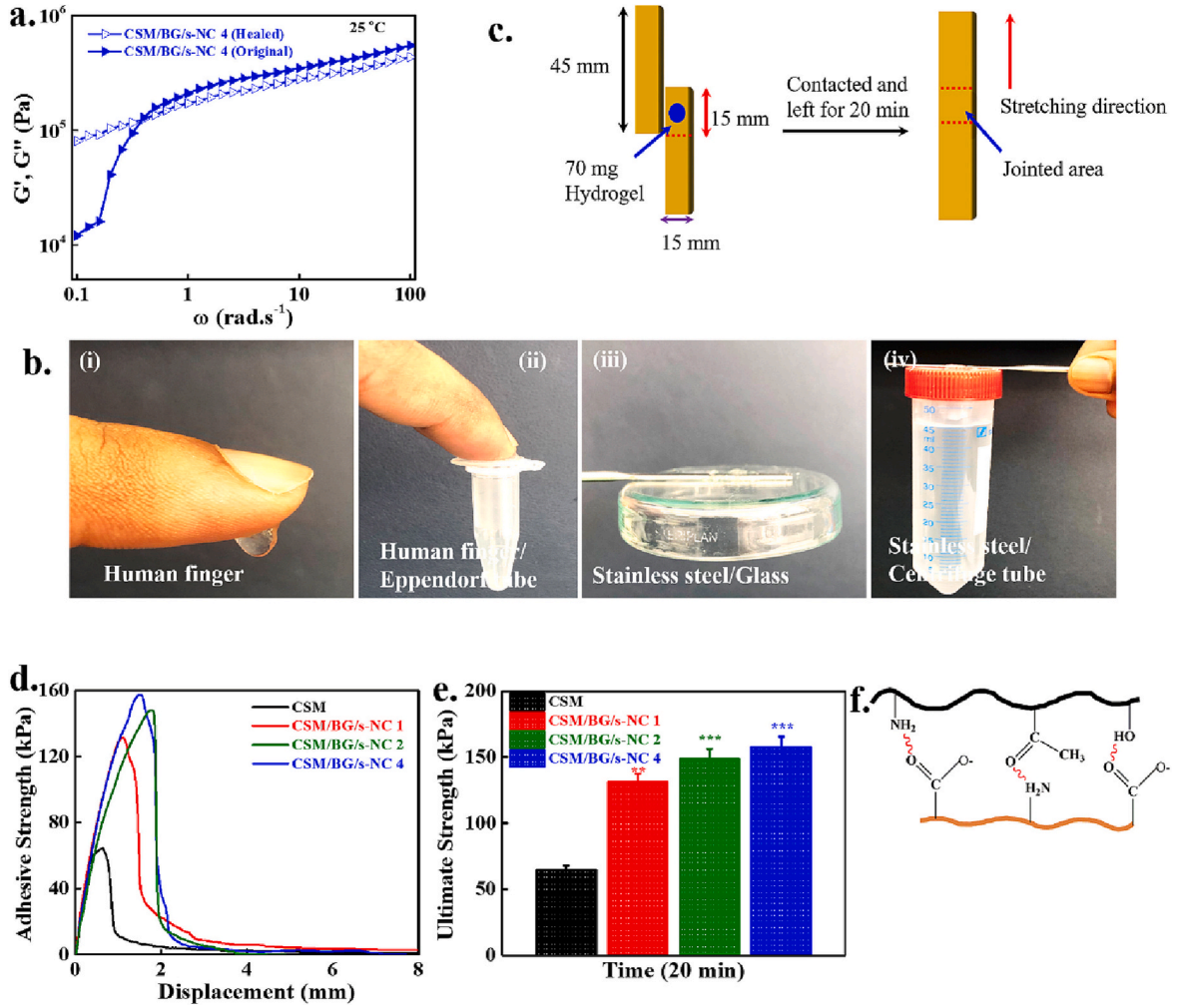

Fig. 5. **(a)** Evaluation of the Self-healing potential of the indicated hydrogel, **(b)** Image of the hydrogels attached to different surfaces, **(c)** schematic presentation of the lap shear method, **(d)** adhesive strength against displacement curves of the hydrogels, **(e)** ultimate adhesive strength of the indicated hydrogels, and **(f)** possible interaction between hydrogels and human skin.

3.5. Biocompatibility and antibacterial interpretation

Examination of hydrogel cytotoxicity is required to assess the compatibility of the materials for personalized healthcare devices. The biocompatibility was evaluated by co-culturing HDF cells with the hydrogels (10 mg) for various periods, and the results are presented in Fig. 6a. Media without hydrogel treatments were used as the controls. No adverse effects on the viability of HDF cells were observed in the presence of the hydrogels. A higher cell viability was observed in the composite hydrogel-treated groups than in the pure polymer and control groups. Cell viability was further increased with an increasing incubation period (3 and 5 d), suggesting improved biocompatibility. This enhancement in cell viability was attributed to the biocompatible s-NC and BG in the polymer matrix, which provided favorable conditions for cellular activity (Coelho et al., 2018; Lee et al., 2019). The cytotoxicity of the hydrogels at a higher concentration (50 mg) was also monitored to examine their dose-dependent cytotoxicity, and the results are shown in Fig. 6b. No adverse effects were observed on the viability of HDF cells and cell viability further increased with an increasing culture time, demonstrating that the hydrogels prompted cellular activity. A slight decrease in cell viability was observed with an increasing nanomaterial content in the polymer matrix. This cytotoxicity might be related to the cellular uptake of nanomaterials. However, the hydrogels still exhibited good viability (>90 %). Li et al. reported the dimension-dependent toxicity of nanocellulose in different cells. They observed that cytotoxicity was significantly affected by the nanocellulose dimensions and cellular uptake and a higher cellular uptake caused significant cytotoxicity (Li et al., 2021). Furthermore, the HDF morphologies within the printed strand were observed after 1 d of incubation to assess the morphological changes of the HDF cells in the presence of printed hydrogel strands, and the images are shown in Fig. 6c. The strands printed from the pure polymer were considered as the controls. In all treatments, the cells were healthy and elongated, confirming the biocompatibility of the printed hydrogels. The composition and concentration of bioink, holding temperature and time profoundly affect the printability of the hydrogels, and, consequently, cell-survival rate. Zhao and coworkers examined the printing parameters on cell survival rate and printability using a microextrusion-based 3D cell printing technology. A decrease in cell survival rate was observed by increasing the bioink concentration, and holding time, as well as decreasing the holding temperature. Thus optimizing the viscoelasticity of the bioink is necessary to achieve better printability, shape fidelity, and cell growth (Zhao et al., 2015).

The antibacterial potential of the hydrogels was monitored against

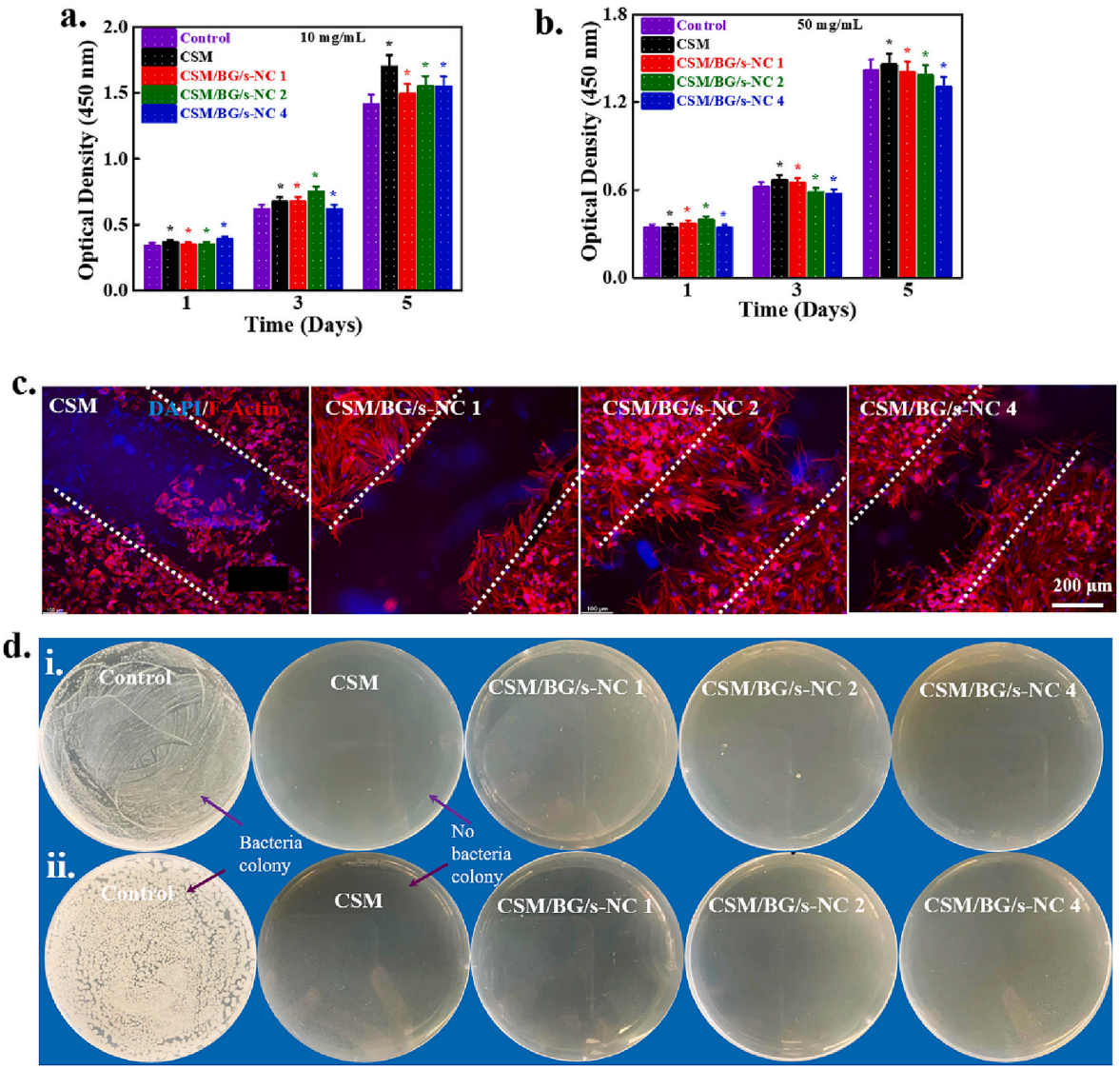

Fig. 6. Biocompatibility examination of the hydrogels. **(a–b)** HDF cell viability at the indicated periods with different concentrations, **(c)** HDF morphologies, and **(d)** antibacterial examination after 24 h of incubation against (i) *E. coli*, and (ii) *S. epidermidis*.

E. coli, as shown in Fig. 6di. The groups without hydrogels treatment were taken as control. Enormous bacteria colonies were observed in the control groups after 24 h of incubation. In contrast, no bacterial colonies were observed in the hydrogels treated groups. The antibacterial potential of the hydrogels was attributed to the positively charged amino functional groups in their structure, which electrostatically interact with the phospholipid components of the bacterial cell membrane and damage them (Patel, Dutta, Ganguly, & Lim, 2021). A similar result was observed with *S. epidermidis* (Gram-positive bacteria) after 24 h of incubation, as shown in Fig. 6dii. These results indicated that the developed hydrogels had antibacterial potential towards Gram-positive and Gram-negative species and could be used for wearable electronic sensors without adding antibiotics.

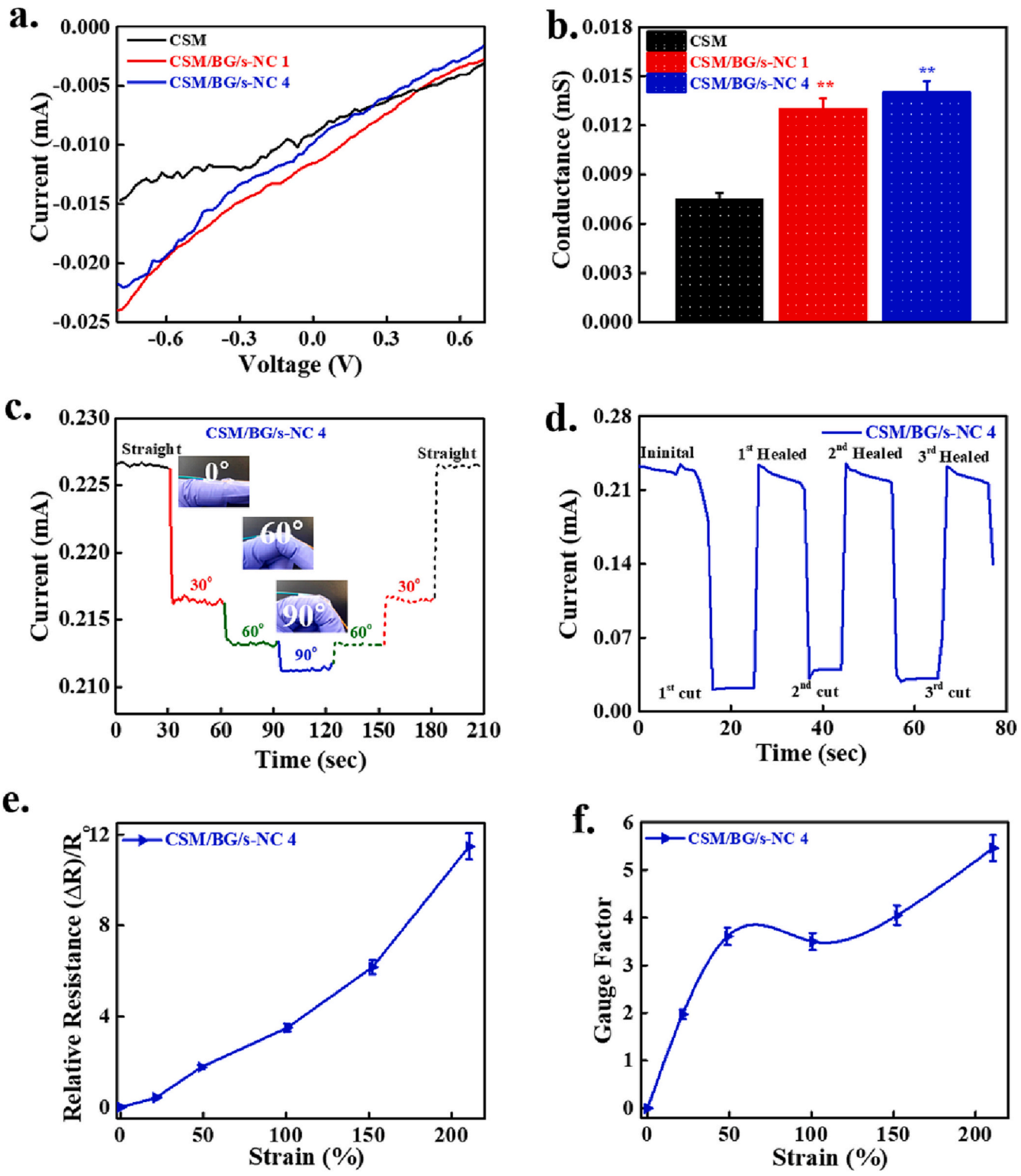

Fig. 7. Electrochemical behavior of the hydrogels. **(a)** Current-voltage curves, **(b)** conductance value of the indicated hydrogels, **(c)** current change at different angles, **(d)** current change during three consecutive cutting and healing processes, **(e)** resistance change with strain, and **(f)** GF of the hydrogel at the indicated strain.

3.6. Electrochemical characteristics of the hydrogels

Conductivity is an essential characteristic of materials for the development of wearable electronic devices for personalized healthcare applications. The electrical conductance of the hydrogels was measured using a Keithley 2460 source meter® at room temperature, and the obtained I-*V* curves are shown in Fig. 7a. The I-V curves presented a linear and non-hysteretic pattern, indicating the electro-conductive characteristics of the hydrogels. The composite hydrogels exhibited improved conductance, as the slope values were 0.007, 0.013, and 0.014 mS for CSM, CSM/BG/s-NC 1, and CSM/BG/s-NC 4, respectively (Fig. 7b). The increased electro-conductivity was attributed to the formation of an efficient ion-conductive pathway in the hydrogels, which accelerated the conduction of ions at the applied voltage. The nanocellulose prepared from the APS hydrolysis generated a negative charge surface owing to the presence of carboxylate groups, which also assisted in generating a conductive pathway (Cheng et al., 2014).

The change in hydrogel current at different bending angles (0, 30, 60, and 90°) on a human finger was examined, and the results are presented in (Fig. 7c). The CSM/BG/s-NC 4 hydrogel was selected for this examination due to its higher electro-conductivity than the other hydrogels. A steady current was observed in the hydrogel under straight conditions, which was significantly decreased with an increasing magnitude of finger bending (0° → 90°). The distance between the active functional groups increased during bending, reducing ion transport and, consequently, increasing resistance (Lu et al., 2021; Zhou et al., 2021). At a high bending angle (90°), the distance between the functional groups increased significantly, causing a significant reduction in the current value. Interestingly, the hydrogel recovered its initial current value after the bending process was reversed (90° → 0°), demonstrating its superior strain-induced current change potential, which was highly beneficial for the development of wearable electronic devices for various applications. The current change in the hydrogel was further analyzed for three successive steps of the cutting and healing process to monitor the influence of the self-healing process on the hydrogel conductivity. As shown in Fig. 7d, the hydrogel exhibited steady current flow under normal conditions, which instantaneously decreased after the hydrogel was cut as the electrical pathway was damaged. The hydrogel rapidly regained its initial current value after healing, demonstrating effective reconstruction of the electrical pathway through the self-healing process. A similar behavior was observed after three consecutive steps, showing that the hydrogel had an excellent self-healing efficiency and could reconstruct the electrical pathway. Hydrogels with self-healing potential are considered attractive platforms for wearable electronic devices because their healing ability can enhance the life span of the devices (Liu et al., 2023; Lo et al., 2021).

The change in the relative resistance of the hydrogel with increasing strain was also measured. As shown in Fig. 7e, a nearly linear increase in the relative resistance was observed with increasing strain, indicating a decrease in the hydrogel current, which was attributed to the weakening of the conduction pathway at a high strain. A relatively small change in resistance (3.4) was observed at a lower strain (100 %), which rapidly increased to 11.5 with increasing strain (210 %). The weakened conducting networks at a strain of 100 % caused a minor change in the current. However, a significant displacement in the conducting networks occurred at a higher strain, leading to a remarkable decrease in the current, and consequently, a rapid increase in the relative resistance (Liu, Chen, et al., 2022). The GF was determined to evaluate the strain sensitivity of the hydrogel by measuring the change in the relative resistance with strain, and the results are shown in Fig. 7f. The GF values were 1.9, 3.5, and 5.6 for 21, 100, and 210 % strains, respectively. The GF systematically increased with increasing strain, suggesting the excellent strain sensitivity of the hydrogel, which was superior to some recently reported nanocellulose-based hydrogels for strain-sensing applications (Cheng et al., 2022; Li et al., 2022; Su et al., 2022; Wang, Xiang, et al., 2021).

3.7. Assessment the sensing abilities of the hydrogel

The real-time sensing abilities of the CSM/BG/s-NC 4 hydrogel were monitored based on their superior electrochemical characteristics. The real-time strain-sensing potential of the hydrogel was examined by placing it at different parts of the human body, including the finger, wrist, and knee. The stretching and bending cycles were conducted to monitor real-time motion. The finger motion waveforms are shown in Fig. 8a. A steady deformation waveform was observed during finger bending and stretching, demonstrating the real-time motion-sensing ability of the hydrogel. The patterns of the generated waveforms were significantly affected by the magnitude of the finger bending and stretching. Compared to the stretching conditions, bending of the finger decreased the current owing to the weakened conducting pathway, as observed in Fig. 7c. The real-time motion-sensing ability of the hydrogel was also monitored on the wrist and knee, and the corresponding waveforms are presented in Fig. 8 b–c. Nearly uniform waveforms were observed during the bending and stretching of the wrist and knee, indicating the high strain sensitivity and good fidelity of the hydrogel for motion sensing applications. These findings demonstrate that CSM/BG/s-NC 4 hydrogel has the potential to be used in wearable electronic devices for strain sensing. We also monitored the motion sensing ability of the pure polymer (CSM) on the human finger to compare the generated patterns with those generated by CSM/BG/s-NC 4 hydrogel, and the result is shown in Fig. S8. CSM produced irregular deformation waveforms when the finger was bent and stretched. It confirmed that adding nanomaterials to form CSM/BG/s-NC 4 composite hydrogel was essential to achieving better sensing ability.

Hydrogels with sign language recognition abilities have received significant attention for the development of wearable electronic devices for different applications. Most electronic devices can only monitor one-dimensional activity, including the motion of different body parts. However, they cannot detect multidimensional sign language. To determine the ability of the composite hydrogel to sense complex spatial movements, the CSM/BG/s-NC 4 was sandwiched between two polyethylene films and connected with a conducting wire. Fig. 8d shows a schematic of the configuration of the sandwiched hydrogel connected to a source meter. The developed platform could provide a precise response to the English letters “K” and “U”. Each letter was written twice to examine the different current changes using CSM and CSM/BG/s-NC 4 hydrogels. As shown in Fig. 8 e–f, the current change was different for each letter, and specific waveforms were generated by individual letters. Similar current changes and waveforms were observed when the same letter was repeatedly written, demonstrating the good reproducibility and sensitivity of the hydrogels. The magnitude of the generated waveforms was significantly affected by the applied pressure, motion tracking, and letter-writing speed (Ge et al., 2019). Due to the improved conductivity, the waveform magnitude generated by the CSM/BG/s-NC 4 hydrogel was significantly higher than that generated by pure CSM. Fig. 8g shows the current change and corresponding waveforms when the letters “KUU” were written together, which were similar to the initial patterns observed in Fig. 8e–f. These findings demonstrated the excellent letter-sensing potential of the developed hydrogel.

The temperature-sensing ability of the hydrogel was further investigated to explore its potential as a “fever indicator.” For this, the hydrogel was placed in a polystyrene “rectangle box” and connected with wires. The entire device was covered with tape to avoid heat loss during measurement. Fig. 8h shows a schematic of the temperature sensing configuration, and Fig. 8i shows the changes in the current of the hydrogel with increasing temperature. The current systematically increased with an increasing temperature (23 °C → 50 °C). The thermo-responsive potential of the hydrogel was attributed to the better entanglements of the polymer chains at higher temperatures, wherein the more effective network structures accelerated the ion transport and consequently increased the conductivity (Wu et al., 2022). Furthermore, the electrical current systematically decreased with decreasing

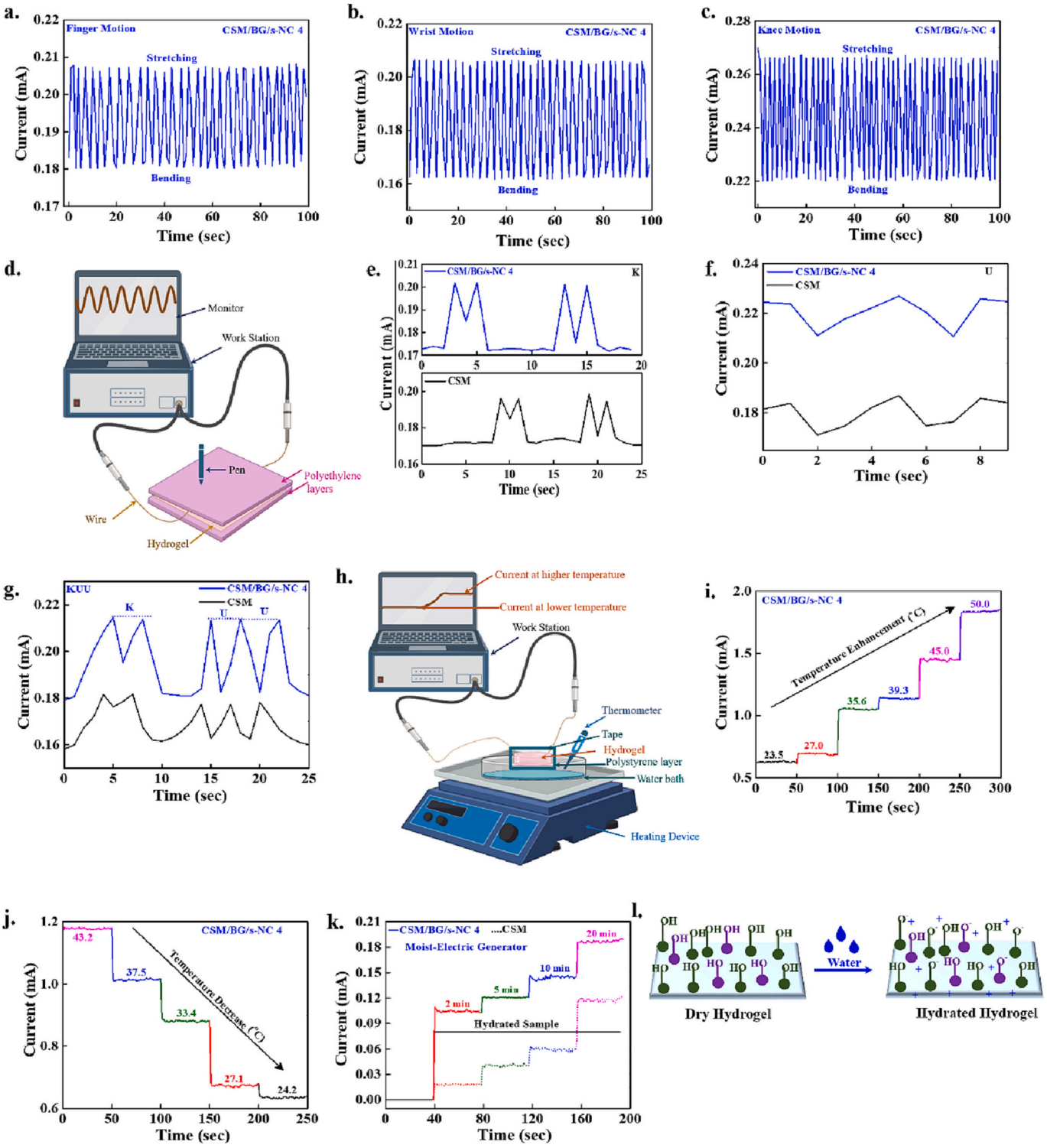

Fig. 8. Examination of the sensing ability of the indicated hydrogels. **(a–c)** Monitoring of the motion sensing at the finger, wrist, and knee, **(d)** schematic presentation for the design of language recognition, **(e–g)** generated waveforms with indicated English letters, **(h)** schematic presentation for temperature sensing, **(i–j)** change in the current value with increasing and decreasing temperature, **(k)** change in the current value in the presence of moisture, and **(l)** possible mechanism for electricity generation.

temperature (43 °C → 24 °C). Fig. 8j shows the changes in the electrical current. Limited ion transport occurred at a lower temperature, enhancing the hydrogel resistance and consequently decreasing the current value. These results indicate that the hydrogel has attractive thermo-responsive potential and can be explored to develop smart electronic devices for personalized healthcare applications.

The composite hydrogel contains many hydroxyl groups from polymers, nanocellulose, and BG. Therefore, it is anticipated that the hydrogel can generate electric power by exchanging protons under moist conditions (Zhang, Zhang, et al., 2021). A dry hydrogel film was soaked in water to examine its moisture-assisted electric generation potential. Fig. 8k shows the changes in the electricity generation of the

hydrogel films (CSM and CSM/BG/s-NC 4) after different soaking periods. No current was observed in the dry hydrogel film, whereas the current was generated in the soaked films and increased with increasing soaking period, indicating its moisture-assisted electric generation potential. The current generation ability of CSM/BG/s-NC 4 was higher than that of the CSM film due to the presence of additional hydroxyl groups from nanocellulose and BG, which facilitated the ion transport.

Fig. 8l presents a possible mechanism for moisture-mediated electricity generation. The hydrogel films remained inactive under dry conditions. After exposure to water, the hydroxyl-rich hydrogel components released many protons that rapidly migrated to generate electricity. Table 1 compares the strain-sensing performance of some previously reported nanocellulose-based hydrogels (Cheng et al., 2022; Cui et al., 2019; Fan et al., 2022; Heidarian et al., 2022; Wang et al., 2022; Zhang et al., 2020; Zhang et al., 2022). Our CSM/BG/s-NC 4 overcomes the disadvantages of reported sensors and demonstrates additional favorable functionalities.

4. Conclusion

Multifunctional, transparent, and printable CSM/nanocellulose/BG hydrogels were developed in an aqueous medium for motion and temperature sensing as well as moisture-assisted electric generation applications. Compared to the pure polymer (CSM), the composite hydrogel exhibited improved porosity and swelling properties. The composite hydrogel had a smaller characteristic length (187.46 nm) than the pure polymer (CSM) hydrogel (195.03 nm), confirming that the interactions between the functionalized polymer chains and the added nanomaterials resulted in assembled structures in the hydrogels. A significant enhancement in the viscoelasticity and recovery strength was observed in the composite hydrogel, further indicating the reinforcing effects of the added nanomaterials.

Improved shape-memory and adhesiveness were observed in the composite hydrogel owing to the abundant active hydroxyl functional groups, which enhanced the adhesiveness by interacting with the functional groups of other surfaces. The developed hydrogel showed biocompatibility with no adverse effects on HDF cells and antibacterial activity against *E. coli* and *S. epidermidis*, which were both favorable for personalized healthcare applications. The composite hydrogel possessed better electro-conductivity than the pure polymer hydrogel (CSM) because the effective conductive pathway accelerated the movement of ions at a particular voltage. The healed hydrogel regained its initial current within a few seconds, indicating its superior self-healing potential. The hydrogel GF values at 100 and 210 % strains were 3.5 and 5.6, respectively.

The real-time motion-sensing ability of the hydrogel was evaluated on various parts of the human body. The generated waveforms were almost identical for all measurements (finger, wrist, and knee), demonstrating their real-time strain-sensing potential. The composite hydrogel exhibited a sign-language recognition ability with good reproducibility and sensitivity. A systematic change in the current was observed with increasing or decreasing temperature, demonstrating its thermo-responsive characteristics. Furthermore, the composite hydrogel showed improved moisture-mediated electricity owing to the large number of hydroxyl groups, which facilitated the movement of protons. Therefore, the multifunctional composite hydrogel developed in this study can be used in wearable electronic devices for personalized healthcare applications.

CRediT authorship contribution statement

Dinesh K. Patel: Conceptualization, Methodology, Investigations, Data curation, *V*isualization, Formal analysis, Writing-original & Revised manuscript. **Tejal V. Patil:** Antibacterial investigation. **Keya Ganguly,** and **Sayan Deb Dutta:** Cytotoxicity evaluation. **Ki-Taek Lim:** Supervision, Funding acquisition, Project administration, Writing-review & editing.

Declaration of competing interest

The authors declare that they have no known competing financial interests or personal relationships that could have appeared to influence the work reported in this paper.

Table 1
A comparative analysis of the strain-sensing potential of some previously reported nanocellulose-based hydrogels with this work.

Hydrogel components	Advantages	Disadvantages	Potential	Ref.
Carboxyl methyl chitosan/ nanocellulose/ chitin nanofibers/tannic acid	3D printable hydrogel, Improved mechanical strength (0.12 → 0.59 MPa) and viscoelasticity (935 → 6923.7 Pa, storage modulus) Adhesiveness with different surfaces (5–24 kPa) and conductive	Longer time for self-healing (12 h) and moderate gauge factor (2.69)	Strain sensor	(Heidarian et al., 2022)
Chitosan/ polyvinyl alcohol/ cyclodextrin	Enhanced mechanical strength (0.5 MPa), and conductivity 2.48 (S m^{-1}) Antibacterial and good strain sensitivity (4.87)	Moderate adhesiveness (2–4 kPa)	Strain sensor	(Fan et al., 2022)
Chitosan/ poly(acrylic acid)/ nanocellulose functionalized with tannic acid	Good mechanical (~0.39 → 1.2 MPa) and recovery strength (90 %), Under-water adhesive and conductive	Moderate adhesiveness (12–19 kPa), Higher time for recovery (60 min), and sensitivity (3.0)	Strain sensor	(Cui et al., 2019)
Polyacrylamide/ sodium alginate/oxidized nanocellulose fibers	Transparent (>84 %) with improved mechanical strength (1.04 MPa), Good stretchability (681 %), anti-freezing, and conductive (1.01 S m^{-1})	Moderate sensitivity (2.1)	Strain sensor	(Cheng et al., 2022)
Carboxymethyl chitosan-g-polyaniline/polyacrylamide/ silver ions	Superior stretchability (~1100 %), and improved mechanical strength (4.78 → 47.2 kPa elastic modulus), and conductive	Moderate adhesiveness (3 → 22 kPa)	Strain sensor	(Zhang et al., 2022)
Polyvinyl alcohol/ carboxymethyl cellulose/ nanocellulose	Transparent (80–86 %), improved mechanical strength (1.4 MPa), and viscoelasticity Anti-freezing (−70 °C) and conductive (0.021 S cm^{-1})	Lower sensitivity (1.4)	Strain sensor	(Wang et al., 2022)
Chitosan citrate/ polysulfobetaine-*co*-acrylic acid	Transparent (>85 %), Improved mechanical strength (0.12 MPa), and recovery potential (~80 % within 8 h) Injectable and conductive (0.11 S m^{-1})	Moderate sensitivity (2.93)	Strain sensor	(Zhang et al., 2020)
Chitosan methacrylamide/ beta glucan/ nanocellulose	Transparent (>85 %), improved viscoelasticity (188.2 → 546.7 kPa, storage modulus), rapid healing (80 % within 10 min), and superior adhesiveness (64.6 → 157.5 kPa) Biocompatible, antibacterial, conductive, and good sensitivity (5.6)	–	Strain, temperature, and moist electric generators	This study

Data availability

Data will be made available on request.

Acknowledgments

We would like to acknowledge the support from the Basic Science Research Program through the National Research Foundation of Korea (NRF) funded by the Ministry of Education (No. 2018R1A6A1A03025582, 2019R1D1A3A03103828, and 2022R1I1A3063302), Republic of Korea.

Appendix A. Supplementary data

Supplementary data to this article can be found online at https://doi.org/10.1016/j.carbpol.2023.120963.

References

Aguayo, M., Fernández Pérez, A., Reyes, G., Oviedo, C., Gacitúa, W., Gonzalez, R., & Uyarte, O. (2018). Isolation and characterization of cellulose nanocrystals from rejected fibers originated in the Kraft pulping process. *Polymers, 10*, 1145.

Ahn, J., Ryu, J., Song, G., Whang, M., & Kim, J. (2019). Network structure and enzymatic degradation of chitosan hydrogels determined by crosslinking methods. *Carbohydrate Polymers, 217*, 160–167.

Alizadehgiashi, M., Nemr, C. R., Chekini, M., Pinto Ramos, D., Mittal, N., Ahmed, S. U., Khuu, N., Kelley, S. O., & Kumacheva, E. (2021). Multifunctional 3D-printed wound dressings. *ACS Nano, 15*, 12375–12387.

Amit, M., Chukoskie, L., Skalsky, A. J., Garudadri, H., & Ng, T. N. (2019). Flexible pressure sensors for objective assessment of motor disorders. *Advanced Functional Materials, 30*, Article 1905241.

Aziz, S. B., Abidin, Z. H. Z., & Kadir, M. F. Z. (2015). Innovative method to avoid the reduction of silver ions to silver nanoparticles (Ag+→Ag0) in silver ion conducting based polymer electrolytes. *Physica Scripta, 90*, Article 035808.

Bagal-Kestwal, D. R., & Chiang, B. H. (2021). Portable paper-micro well device composed of agglomerated nano-hematite clusters in enzyme-hydrogel composite for beta glucan detection using smartphone. *Sensors and Actuators B: Chemical, 339*, Article 129836.

Chakraborty, P., Guterman, T., Adadi, N., Yadid, M., Brosh, T., Adler-Abramovich, L., Dvir, T., & Gazit, E. (2018). A self-healing, all-organic, conducting, composite peptide hydrogel as pressure sensor and electrogenic cell soft substrate. *ACS Nano, 13*, 163–175.

Cheng, M., Qin, Z., Liu, Y., Qin, Y., Li, T., Chen, L., & Zhu, M. (2014). Efficient extraction of carboxylated spherical cellulose nanocrystals with narrow distribution through hydrolysis of lyocell fibers by using ammonium persulfate as an oxidant. *Journal of Materials Chemistry A, 2*, 251–258.

Cheng, Y., Zang, J., Zhao, X., Wang, H., & Hu, Y. (2022). Nanocellulose-enhanced organohydrogel with high-strength, conductivity, and anti-freezing properties for wearable strain sensors. *Carbohydrate Polymers, 277*, Article 118872.

Coelho, C. C. S., Michelin, M., Cerqueira, M. A., Gonçalves, C., Tonon, R. V., Pastrana, L. M., Freitas-Silva, O., Vicente, A. A., Cabral, L. M. C., & Teixeira, J. A. (2018). Cellulose nanocrystals from grape pomace: Production, properties and cytotoxicity assessment. *Carbohydrate Polymers, 192*, 327–336.

Cong, Y., Liu, S., Wu, F., Zhang, H., & Fu, J. (2020). Shape memory effect and rapid reversible actuation of nanocomposite hydrogels with electrochemically controlled local metal ion coordination and crosslinking. *Journal of Materials Chemistry B, 8*, 9679–9685.

Cui, C., Shao, C., Meng, L., & Yang, J. (2019). High-strength, self-adhesive, and strain-sensitive chitosan/poly(acrylic acid) double-network nanocomposite hydrogels fabricated by salt-soaking strategy for flexible sensors. *ACS Applied Materials & Interfaces, 11*, 39228–39237.

Dang, C., Wang, M., Yu, J., Chen, Y., Zhou, S., Feng, X., Liu, D., & Qi, H. (2019). Transparent, highly stretchable, rehealable, sensing, and fully recyclable ionic conductors fabricated by one-step polymerization based on a small biological molecule. *Advanced Functional Materials, 29*, Article 1902467.

Dong, S., Feng, S., Liu, F., Li, R., Li, W., Liu, F., Shi, G., Chen, L., & Zhang, Y. (2021). Factors influencing the adhesive behavior of carboxymethyl cellulose-based hydrogel for food applications. *International Journal of Biological Macromolecules, 179*, 398–406.

Doshi, B., Repo, E., Heiskanen, J. P., Sirviö, J. A., & Sillanpää, M. (2017). Effectiveness of N, O-carboxymethyl chitosan on destabilization of marine diesel, diesel and marine-2T oil for oil spill treatment. *Carbohydrate Polymers, 167*, 326–336.

Dutta, S. D., Hexiu, J., Patel, D. K., Ganguly, K., & Lim, K.-T. (2021). 3D-printed bioactive and biodegradable hydrogel scaffolds of alginate/gelatin/cellulose nanocrystals for tissue engineering. *International Journal of Biological Macromolecules, 167*, 644–658.

El Hosary, R., El-Mancy, S. M. S., El Deeb, K. S., Eid, H. H., El Tantawy, M. E., Shams, M. M., Samir, R., Assar, N. H., & Sleem, A. A. (2020). Efficient wound healing composite hydrogel using egyptian Avena sativa L. Polysaccharide containing β-glucan. *International Journal of Biological Macromolecules, 149*, 1331–1338.

Fan, X., Zhao, L., Ling, Q., & Gu, H. (2022). Tough, self-adhesive, antibacterial, and recyclable supramolecular double network flexible hydrogel sensor based on PVA/Chitosan/Cyclodextrin. *Industrial & Engineering Chemistry Research, 61*, 3620–3635.

Gamage, S., Kang, E. S. H., Åkerlind, C., Sardar, S., Edberg, J., Kariis, H., Ederth, T., Berggren, M., & Jonsson, M. P. (2020). Transparent nanocellulose metamaterial enables controlled optical diffusion and radiative cooling. *Journal of Materials Chemistry C, 8*, 11687–11694.

Gao, T., Gillispie, G. J., Copus, J. S., Pr, A. K., Seol, Y.-J., Atala, A., Yoo, J. J., & Lee, S. J. (2018). Optimization of gelatin–alginate composite bioink printability using rheological parameters: A systematic approach. *Biofabrication, 10*, Article 034106.

Ge, G., Lu, Y., Qu, X., Zhao, W., Ren, Y., Wang, W., Wang, Q., Huang, W., & Dong, X. (2019). Muscle-inspired self-healing hydrogels for strain and temperature sensor. *ACS Nano, 14*, 218–228.

Guo, B., Qu, J., Zhao, X., & Zhang, M. (2019). Degradable conductive self-healing hydrogels based on dextran-graft-tetraaniline and N-carboxyethyl chitosan as injectable carriers for myoblast cell therapy and muscle regeneration. *Acta Biomaterialia, 84*, 180–193.

He, Y., Deng, Z., Wang, Y.-J., Zhao, Y., & Chen, L. (2022). Polysaccharide/Ti3C2Tx MXene adhesive hydrogels with self-healing ability for multifunctional and sensitive sensors. *Carbohydrate Polymers, 291*, Article 119572.

Heidarian, P., Gharaie, S., Yousefi, H., Paulino, M., Kaynak, A., Varley, R., & Kouzani, A. Z. (2022). A 3D printable dynamic nanocellulose/nanochitin self-healing hydrogel and soft strain sensor. *Carbohydrate Polymers, 291*, Article 119545.

Heiner, B. R., Pittsford, A. M., & Kandel, S. A. (2023). Self-assembly controlled at the level of individual functional groups. *Chemical Communications, 59*, 170–178.

Jeong, Y. R., Oh, S. Y., Kim, J. W., Jin, S. W., & Ha, J. S. (2020). A highly conductive and electromechanically self-healable gold nanosheet electrode for stretchable electronics. *Chemical Engineering Journal, 384*, Article 123336.

Jing, H., He, L., Feng, J., Fu, H., Guan, S., & Guo, P. (2019). High strength hydrogels with multiple shape-memory ability based on hydrophobic and electrostatic interactions. *Soft Matter, 15*, 5264–5270.

Kolawole, O. M., Lau, W. M., & Khutoryanskiy, V. V. (2018). Methacrylated chitosan as a polymer with enhanced mucoadhesive properties for transmucosal drug delivery. *International Journal of Pharmaceutics, 550*, 123–129.

Lee, K., Kwon, Y., Hwang, J., Choi, Y., Kim, K., Koo, H.-J., Seo, Y., Jeon, H., & Choi, J. (2019). Synthesis and functionalization of β-glucan particles for the effective delivery of doxorubicin molecules. *ACS Omega, 4*, 668–674.

Li, H., Yang, Y., Li, M., Zhu, Y., Zhang, C., Zhang, R., & Song, Y. (2022). Frost-resistant and ultrasensitive strain sensor based on a tannic acid-nanocellulose/sulfonated carbon nanotube-reinforced polyvinyl alcohol hydrogel. *International Journal of Biological Macromolecules, 219*, 199–212.

Li, J., Wang, X., Chang, C. H., Jiang, J., Liu, Q., Liu, X., Liao, Y. P., Ma, T., Meng, H., & Xia, T. (2021). Nanocellulose length determines the differential cytotoxic effects and inflammatory responses in macrophages and hepatocytes. *Small, 17*, Article 2102545.

Li, L., Yan, B., Yang, J., Chen, L., & Zeng, H. (2015). Novel mussel-inspired injectable self-healing hydrogel with anti-biofouling property. *Advanced Materials, 27*, 1294–1299.

Li, M., Chen, S., Fan, B., Wu, B., & Guo, X. (2020a). Printed flexible strain sensor Array for bendable interactive surface. *Advanced Functional Materials, 30*, Article 2003214.

Li, M., Fu, S., Lucia, L. A., & Wang, Y. (2020b). Ultra-efficient photo-triggerable healing and shape-memory nanocomposite materials doped with copper sulfide nanoparticles. *Composites Science and Technology, 199*, Article 108371.

Liang, L., Lv, H., Shi, X.-L., Liu, Z., Chen, G., Chen, Z.-G., & Sun, G. (2021). A flexible quasi-solid-state thermoelectrochemical cell with high stretchability as an energy-autonomous strain sensor. *Materials Horizons, 8*, 2750–2760.

Liang, R., Yu, H., Wang, L., Lin, L., Wang, N., & Naveed, K.-U.-R. (2019). Highly tough hydrogels with the body temperature-responsive shape memory effect. *ACS Applied Materials & Interfaces, 11*, 43563–43572.

Liu, D., Dong, X., Han, B., Huang, H., & Qi, M. (2020). Cellulose nanocrystal/collagen hydrogels reinforced by anisotropic structure: Shear viscoelasticity and related strengthening mechanism. *Composites Communications, 21*, Article 100374.

Liu, H., Yu, L., Zhao, B., Ni, Y., Gu, P., Qiu, H., Zhang, W., & Chen, K. (2023). Bio-inspired color-changing and self-healing hybrid hydrogels for wearable sensors and adaptive camouflage. *Journal of Materials Chemistry C, 11*, 285–298.

Liu, J., Chen, X., Sun, B., Guo, H., Guo, Y., Zhang, S., Tao, R., Yang, Q., & Tang, J. (2022a). Stretchable strain sensor of composite hydrogels with high fatigue resistance and low hysteresis. *Journal of Materials Chemistry A, 10*, 25564–25574.

Liu, L., Niu, S., Zhang, J., Mu, Z., Li, J., Li, B., Meng, X., Zhang, C., Wang, Y., Hou, T., et al. (2022b). Bioinspired, omnidirectional, and hypersensitive flexible strain sensors. *Advanced Materials, 34*, Article 2200823.

Liu, M., Liu, P., Lu, G., Xu, Z., & Yao, X. (2018). Multiphase-assembly of siloxane oligomers with improved mechanical strength and water-enhanced healing. *Angewandte Chemie International Edition, 57*, 11242–11246.

Liu, Y., Wang, L., Mi, Y., Zhao, S., Qi, S., Sun, M., Peng, B., Xu, Q., Niu, Y., & Zhou, Y. (2022c). Transparent stretchable hydrogel sensors: Materials, design and applications. *Journal of Materials Chemistry C, 10*, 13351–13371.

Lo, C.-Y., Zhao, Y., Kim, C., Alsaid, Y., Khodambashi, R., Peet, M., Fisher, R., Marvi, H., Berman, S., Aukes, D., et al. (2021). Highly stretchable self-sensing actuator based on conductive photothermally-responsive hydrogel. *Materials Today, 50*, 35–43.

Lu, F., Wang, Y., Wang, C., Kuga, S., Huang, Y., & Wu, M. (2020). Two-dimensional nanocellulose-enhanced high-strength, self-adhesive, and strain-sensitive Poly (acrylic acid) hydrogels fabricated by a radical-induced strategy for a skin sensor. *ACS Sustainable Chemistry & Engineering, 8*, 3427–3436.

Lu, Y., Yue, Y., Ding, Q., Mei, C., Xu, X., Wu, Q., Xiao, H., & Han, J. (2021). Self-recovery, fatigue-resistant, and multifunctional sensor assembled by a nanocellulose/carbon

nanotube nanocomplex-mediated hydrogel. *ACS Applied Materials & Interfaces, 13*, 50281–50297.
Lungu, A., Cernencu, A. I., Dinescu, S., Balahura, R., Mereuta, P., Costache, M., Syverud, K., Stancu, I. C., & Iovu, H. (2021). Nanocellulose-enriched hydrocolloid-based hydrogels designed using a Ca2+ free strategy based on citric acid. *Materials & Design, 197*, Article 109200.
Malekpour, A., & Chen, X. (2022). Printability and cell viability in extrusion-based bioprinting from experimental, computational, and machine learning views. *Journal of Functional Biomaterials, 13*, 40.
Nissenbaum, A., Greenfeld, I., & Wagner, H. D. (2020). Shape memory polyurethane - amorphous molecular mechanism during fixation and recovery. *Polymer, 190*, Article 122226.
Patel, D. K., Dutta, S. D., Ganguly, K., & Lim, K.-T. (2021a). Multifunctional bioactive chitosan/cellulose nanocrystal scaffolds eradicate bacterial growth and sustain drug delivery. *International Journal of Biological Macromolecules, 170*, 178–188.
Patel, D. K., Dutta, S. D., Hexiu, J., Ganguly, K., & Lim, K.-T. (2022a). 3D-printable chitosan/silk fibroin/cellulose nanoparticle scaffolds for bone regeneration via M2 macrophage polarization. *Carbohydrate Polymers, 281*, Article 119077.
Patel, D. K., Dutta, S. D., & Lim, K.-T. (2019). Nanocellulose-based polymer hybrids and their emerging applications in biomedical engineering and water purification. *RSC Advances, 9*, 19143–19162.
Patel, D. K., Dutta, S. D., Shin, W.-C., Ganguly, K., & Lim, K.-T. (2021b). Fabrication and characterization of 3D printable nanocellulose-based hydrogels for tissue engineering. *RSC Advances, 11*, 7466–7478.
Patel, D. K., Ganguly, K., Dutta, S. D., Patil, T. V., & Lim, K.-T. (2022b). Multifunctional hydrogels of polyvinyl alcohol/polydopamine functionalized with carbon nanomaterials as flexible sensors. *Materials Today Communications, 32*, Article 103906.
Patel, D. K., Ganguly, K., Dutta, S. D., Patil, T. V., & Lim, K.-T. (2023a). Cellulose nanocrystals vs. Cellulose nanospheres: A comparative study of cytotoxicity and macrophage polarization potential. *Carbohydrate Polymers, 303*, Article 120464.
Patel, D. K., Ganguly, K., Dutta, S. D., Patil, T. V., Randhawa, A., & Lim, K.-T. (2023b). Highly stretchable, adhesive, and biocompatible hydrogel platforms of tannic acid functionalized spherical nanocellulose for strain sensors. *International Journal of Biological Macromolecules, 229*, 105–122.
Patel, D. K., Ganguly, K., Hexiu, J., Dutta, S. D., Patil, T. V., & Lim, K.-T. (2022c). Functionalized chitosan/spherical nanocellulose-based hydrogel with superior antibacterial efficiency for wound healing. *Carbohydrate Polymers, 284*, Article 119202.
Patel, D. K., Seo, Y.-R., Dutta, S. D., Lee, O. H., & Lim, K.-T. (2020). Influence of maitake (Grifola frondosa) particle sizes on human mesenchymal stem cells and in vivo evaluation of their therapeutic potential. *BioMed Research International, 2020*, 1–13.
Pati, F., Jang, J., Ha, D.-H., Won Kim, S., Rhie, J.-W., Shim, J.-H., Kim, D.-H., & Cho, D.-W. (2014). Printing three-dimensional tissue analogues with decellularized extracellular matrix bioink. *Nature Communications*, 5.
Qu, X., Wang, S., Zhao, Y., Huang, H., Wang, Q., Shao, J., Wang, W., & Dong, X. (2021). Skin-inspired highly stretchable, tough and adhesive hydrogels for tissue-attached sensor. *Chemical Engineering Journal, 425*, Article 131523.
Roy, A., Manna, K., Ray, P. G., Dhara, S., & Pal, S. (2022). β-cyclodextrin-based ultrahigh stretchable, flexible, electro- and pressure-responsive, adhesive, transparent hydrogel as motion sensor. *ACS Applied Materials & Interfaces, 14*, 17065–17080.
Schwab, A., Levato, R., D'Este, M., Piluso, S., Eglin, D., & Malda, J. (2020). Printability and shape Fidelity of bioinks in 3D bioprinting. *Chemical Reviews, 120*, 11028–11055.
Shan, L., Tian, Y., Jiang, J., Zhang, X., & Meng, Y. (2015). Effects of pH on shear thinning and thickening behaviors of fumed silica suspensions. *Colloids and Surfaces A: Physicochemical and Engineering Aspects, 464*, 1–7.
Shang, J., Le, X., Zhang, J., Chen, T., & Theato, P. (2019). Trends in polymeric shape memory hydrogels and hydrogel actuators. *Polymer Chemistry, 10*, 1036–1055.
Song, Y., Chen, Y., Chen, R., Zhang, H., Shi, D., Wang, Y., Dong, W., Ma, P., & Zhao, Y. (2021). Use of quadruple hydrogen bonding as the switching phase in thermo- and light-responsive shape memory hydrogel. *ACS Applied Polymer Materials, 3*, 2884–2888.
Su, J., Zhang, L., Wan, C., Deng, Z., Wei, S., Yong, K.-T., & Wu, Y. (2022). Dual-network self-healing hydrogels composed of graphene oxide@nanocellulose and poly(AAm-co-AAc). *Carbohydrate Polymers, 296*, Article 119905.
Sun, Z., Hu, Y., Wei, C., Hao, R., Hao, C., Liu, W., Liu, H., Huang, M., He, S., & Yang, M. (2022). Transparent, photothermal and stretchable alginate-based hydrogels for remote actuation and human motion sensing. *Carbohydrate Polymers, 293*, Article 119727.
Tan, J., Huang, C., Liu, D., Zhang, X., Bai, Y., & Zhang, L. (2016). Alcoholic photoinitiated polymerization-induced self-assembly (Photo-PISA): A fast route toward Poly(isobornyl acrylate)-based diblock copolymer nano-objects. *ACS Macro Letters, 5*, 894–899.
Trache, D., Tarchoun, A. F., Derradji, M., Hamidon, T. S., Masruchin, N., Brosse, N., & Hussin, M. H. (2020). Nanocellulose: From fundamentals to advanced applications. *Frontiers in Chemistry*, 8.
Wang, B., Dai, L., Hunter, L. A., Zhang, L., Yang, G., Chen, J., Zhang, X., He, Z., & Ni, Y. (2021a). A multifunctional nanocellulose-based hydrogel for strain sensing and self-powering applications. *Carbohydrate Polymers, 268*, Article 118210.
Wang, H., Li, Z., Zuo, M., Zeng, X., Tang, X., Sun, Y., & Lin, L. (2022). Stretchable, freezing-tolerant conductive hydrogel for wearable electronics reinforced by cellulose nanocrystals toward multiple hydrogen bonding. *Carbohydrate Polymers, 280*, Article 119018.
Wang, S., Li, S., & Gao, L. (2019). Dispersed Association of Single-Component Short-Alkyl Chains toward thermally programmable and malleable multiple-shape hydrogel. *ACS Applied Materials & Interfaces, 11*, 43622–43630.
Wang, S., Oh, J. Y., Xu, J., Tran, H., & Bao, Z. (2018a). Skin-inspired electronics: An emerging paradigm. *Accounts of Chemical Research, 51*, 1033–1045.
Wang, S., Xiang, J., Sun, Y., Wang, H., Du, X., Cheng, X., Du, Z., & Wang, H. (2021b). Skin-inspired nanofibrillated cellulose-reinforced hydrogels with high mechanical strength, long-term antibacterial, and self-recovery ability for wearable strain/pressure sensors. *Carbohydrate Polymers, 261*, Article 117894.
Wang, Z., Zhou, H., Lai, J., Yan, B., Liu, H., Jin, X., Ma, A., Zhang, G., Zhao, W., & Chen, W. (2018b). Extremely stretchable and electrically conductive hydrogels with dually synergistic networks for wearable strain sensors. *Journal of Materials Chemistry C, 6*, 9200–9207.
Wu, S., Wang, T.-W., Du, Y., Yao, B., Duan, S., Yan, Y., Hua, M., Alsaid, Y., Zhu, X., & He, X. (2022). Tough, anti-freezing and conductive ionic hydrogels. *NPG Asia Materials, 14*.
Xu, J., Wong, C.-W., & Hsu, S.-H. (2020). An injectable, electroconductive Hydrogel/Scaffold for neural repair and motion sensing. *Chemistry of Materials, 32*, 10407–10422.
Xu, Q., Ji, Y., Sun, Q., Fu, Y., Xu, Y., & Jin, L. (2019). Fabrication of cellulose Nanocrystal/Chitosan hydrogel for controlled drug release. *Nanomaterials, 9*, 253.
Zanon, M., Chiappone, A., Garino, N., Canta, M., Frascella, F., Hakkarainen, M., Pirri, C. F., & Sangermano, M. (2022). Microwave-assisted methacrylation of chitosan for 3D printable hydrogels in tissue engineering. *Materials Advances, 3*, 514–525.
Zhang, G.-H., Zhang, L., Zhu, Q.-H., Chen, H., Yuan, W.-L., Fu, J., Wang, S.-L., He, L., & Tao, G.-H. (2021a). Self-healable, malleable, and flexible ionic polyimine as an environmental sensor for portable exogenous pollutant detection. *ACS Materials Letters, 4*, 136–144.
Zhang, H., Shen, H., Lan, J., Wu, H., Wang, L., & Zhou, J. (2022). Dual-network polyacrylamide/carboxymethyl chitosan-grafted-polyaniline conductive hydrogels for wearable strain sensors. *Carbohydrate Polymers, 295*, Article 119848.
Zhang, J., Chen, L., Shen, B., Wang, Y., Peng, P., Tang, F., & Feng, J. (2020). Highly transparent, self-healing, injectable and self-adhesive chitosan/polyzwitterion-based double network hydrogel for potential 3D printing wearable strain sensor. *Materials Science and Engineering: C, 117*, Article 111298.
Zhang, X., Sheng, N., Wang, L., Tan, Y., Liu, C., Xia, Y., Nie, Z., & Sui, K. (2019). Supramolecular nanofibrillar hydrogels as highly stretchable, elastic and sensitive ionic sensors. *Materials Horizons, 6*, 326–333.
Zhang, Y., MohebbiPour, A., Mao, J., Mao, J., & Ni, Y. (2021b). Lignin reinforced hydrogels with multi-functional sensing and moist-electric generating applications. *International Journal of Biological Macromolecules, 193*, 941–947.
Zhao, Y., Li, Y., Mao, S., Sun, W., & Yao, R. (2015). The influence of printing parameters on cell survival rate and printability in microextrusion-based 3D cell printing technology. *Biofabrication, 7*, Article 045002.
Zhou, Y., Wang, F., Yang, Z., Hu, X., Pan, Y., Lu, Y., & Jiang, M. (2022). 3D printing of polyurethane/nanocellulose shape memory composites with tunable glass transition temperature. *Industrial Crops and Products, 182*, Article 114831.
Zhou, Z., He, Z., Yin, S., Xie, X., & Yuan, W. (2021). Adhesive, stretchable and antibacterial hydrogel with external/self-power for flexible sensitive sensor used as human motion detection. *Composites Part B: Engineering, 220*, Article 108984.
Zhu, X., Qi, P., Fan, W., Wang, H., & Sui, K. (2022). Bioinspired multifunctional self-powered ionic receptors derived by gradient polyelectrolyte hydrogels. *Chemical Engineering Journal, 438*, Article 135610.